

A Study of Hole Transport in Crystalline Monoclinic Selenium Using
Bulk Monte Carlo Techniques

by

Atreyo Mukherjee

A Thesis Presented in Partial Fulfillment
of the Requirements for the Degree
Master of Science

Approved November 2017 by the
Graduate Supervisory Committee:

Dragica Vasileska , Co-chair
Amirhossein Goldan , Co-chair
Stephen Goodnick

ARIZONA STATE UNIVERSITY

December 2017

ABSTRACT

Amorphous materials can be uniformly deposited over a large area at lower cost compared to crystalline semiconductors (Silicon or Germanium). This property along with its high resistivity and wide band-gap found many applications in devices like rectifiers, xerography, xero-radiography, ultrahigh sensitivity optical cameras, digital radiography, and mammography (2D and 3D tomosynthesis). Amorphous selenium is the only amorphous material that undergoes impact ionization where only holes avalanche at high electric fields. This leads to a small excess noise factor which is a very important performance comparison matrix for avalanche photodetectors. Thus, there is a need to model high field avalanche process in amorphous selenium. At high fields, the transport in amorphous selenium changes from low values of activated trap-limited drift mobility to higher values of band transport mobility, via extended states. When the transport shifts from activated mobility with a high degree of localization to extended state band transport, the wavefunction of the amorphous material resembles that of its crystalline counterpart. To that effect, crystalline monoclinic selenium which has the closest resemblance to vapor deposited amorphous selenium has been studied. Modelling a crystalline semiconductor makes calculations simpler. The transport phenomena in crystalline monoclinic selenium is studied by using a bulk Monte Carlo technique to solve the semi-classical Boltzmann Transport equation and thus calculate vital electrical parameters like mobility, critical field and mobility variations against temperatures. The band structure and the density of states function for monoclinic selenium was obtained by using an atomistic simulation tool, the Atomistic Toolkit in the Virtual Nano Lab, Quantum Wise, Copenhagen, Denmark. Moreover, the velocity and energy against time characteristics have been simulated for a wide range of electric fields ($1-1000 \frac{kV}{cm}$), which is further used to find the hole drift mobility. The low field mobility is obtained from the slope of the velocity vs.

electric field plot. The low field hole mobility was calculated to be $5.51 \frac{cm^2}{Vs}$ at room temperature. The experimental value for low field hole mobility is $7.29 \frac{cm^2}{Vs}$. The energy versus electric field simulation at high fields is used to match the experimental onset of avalanche ($754 \frac{kV}{cm}$) for an ionization threshold energy of 2.1 eV. The Arrhenius plot for mobility against temperature is simulated and compared with published experimental data. The experimental and simulation results show a close match, thus validating the study.

Dedicated to my teachers, parents, colleagues and friends.

ACKNOWLEDGMENTS

I would like to thank my guide and mentor Dr. Dragica Vasileska for her support and motivation. Without her support, it would have been impossible to complete this MS thesis. Her trust and confidence, helped me successfully accomplish my goals. I learn from every interaction I have with her. I would also like to thank my co-guide Dr. Amirhossein Goldan in the Department of Radiology, Stony Brook Medicine for his help, co-operation and insight into the physics of amorphous semiconductors. Without him, this project would not have been possible . I would also like to thank Dr. Stephen Goodnick , for being an inspiration and also a part of my Graduate Advisory Committee .

For running some of the density functional theory (DFT) simulations, this research used the computational resources of the Center for Functional Nanomaterials (CFN), which is a U.S. DOE Office of Science Facility, at Brookhaven National Laboratory (BNL) under Contract No. DE-SC0012704.

I am grateful to Dr. Garrett Schlenvogt, senior TCAD Applications Engineer, Silvaco, Inc, for motivating me throughout and helping me believe in myself. I am grateful to my academic advisor Toni Mengert for helping me out with all the administrative formalities. I am also grateful to all the members of my research group for being supportive and encouraging me to improve my skills. I am indebted to my parents for the love and support I received from them. I would like to express my deepest love and gratitude to my elder brother , Dr. Arghya Mukherjee for being an inspiration and role model, to take up engineering as a career.

TABLE OF CONTENTS

	Page
LIST OF TABLES	vii
LIST OF FIGURES	viii
CHAPTER	
1 INTRODUCTION	1
1.1 Why Amorphous Selenium?	4
1.2 Monoclinic vs Trigonal Selenium	7
1.3 Organization of Thesis	9
2 BAND STRUCTURE AND DENSITY OF STATES CALCULATIONS USING DENSITY FUNCTIONAL THEORY	11
2.1 Charge Transport In Amorphous Selenium	12
2.2 Band Structure	15
2.3 Density of states Calculations	16
3 SCATTERING MECHANISMS IN MONOCLINIC SELENIUM	18
3.1 Fermi's Golden Rule	19
3.2 Acoustic Scattering	20
3.3 Non-polar Optical scattering	24
4 BULK MONTE CARLO THEORY	27
4.1 Bulk Monte Carlo Algorithm	29
4.2 Parameters Initialization	29
4.3 Scattering Table Construction	31
4.4 Carrier Initialization	32
4.5 Histogram Calculation	32
4.6 Free-Flight Scatter Subroutine	33
5 RESULTS AND CONCLUSIONS	37

CHAPTER	Page
5.1 Initial Histograms	37
5.2 Final Histograms	39
5.3 Scattering Rates	42
5.4 Energy and Velocity vs. Time Characteristics	42
5.5 Energy and Velocity vs. Electric Field Characteristics	42
5.6 Mobility vs. Temperature	45
5.7 Conclusions	46
BIBLIOGRAPHY	49

LIST OF TABLES

Table	Page
5.1 Bulk Monte Carlo Parameters	37
5.2 A Comparison Between Experimental and Simulated Mobility for M-selenium Tabulated Against Temperature.	48

LIST OF FIGURES

Figure	Page
1.1 (a) Periodic Wavefunction for a Crystalline Lattice. (b) Extended Wavefunction in a Random Potential for $E > E_C$. (c) Quasi-Extended Wavefunction for $E \approx EC$. (d) Localized Wavefunction with an Exponentially Decaying Envelope for $E < E_C$. (e) Strongly Localized Wavefunctions $E \ll E_C$	5
1.2 Direct Conversion Flat Panel Detector (<i>FPD</i>) for Digital Radiography Made Using A-Selenium	7
1.3 (a) The First Medical X-ray Image Taken (b) X-ray Image Taken with a Modern Day Imager	8
1.4 (a) Unit Cell T-selenium With Polymeric Chains Se_n . (b) Unit Cell M-selenium With Monomer Rings Se_8	9
2.1 (a) Band Vs Brownian Vs Hopping Transport (b) Density of States.	13
2.2 Crystallographic File for Alpha M-selenium Showing Se_8 Rings.	16
2.3 (a) Band-structure of Alpha M-selenium (b) Direct Band-gap Showing a Value of 2.126 eV.	17
2.4 Density of States for M-Selenium.	17
3.1 Valence Band Dos for M-selenium. 0 In the Energy Axis Refers to the Top of the Valence Band.	19
3.2 Fractional Change in Length Due to Strain Tensor	21
3.3 Deformation Potential Squared vs. Energy	24
3.4 Acoustic Scattering Rate (Log Scale) vs. Energy.	24
3.5 Non-polar Optical Scattering Rate (Log Scale) vs. Energy	26
4.1 Shows Three Dimensional Processes Namely Drift Diffusion and Collision in Two Dimensional Space.	28

Figure	Page
4.2 Bulk Monte Carlo Algorithm	30
4.3 Scattering Table Creation.....	31
4.4 Free-Flight Scatter Representation of the Monte Carlo Method.....	33
4.5 Free-Flight Scatter Subroutine in One Flowchart	36
5.1 Histogram Showing the Initial Carrier Energy Distribution.....	38
5.2 Histogram Showing the Initial Carrier Wave Vector (k_x [1/m]) Distri- bution.....	39
5.3 Histogram Showing the Initial Carrier Wave Vector (k_y [1/m]) Distri- bution.....	39
5.4 Histogram Showing the Initial Carrier Wave Vector (k_z [1/m]) Distri- bution.....	40
5.5 Histogram Showing the Final Carrier Energy Distribution at an Elec- tric Field of $50\frac{kV}{cm}$	40
5.6 Histogram Showing the Final Carrier Wave Vector (k_x) Distribution at an Electric Field of $50\frac{kV}{cm}$	41
5.7 Histogram Showing the Final Carrier Wave Vector (k_y) Distribution at an Electric Field of $50\frac{Kv}{cm}$	41
5.8 Histogram Showing the Final Carrier Wave Vector (k_z) Distribution at an Electric Field of $50\frac{Kv}{cm}$	41
5.9 Scattering Rates (1/s) in Log Scale vs. Energy	42
5.10 Drift Velocity vs. Time Characteristics.....	43
5.11 Energy vs.Time Characteristics.....	43
5.12 Drift Velocity vs. Electric Field	44
5.13 Energy vs. High Electric Field	44

5.14 Histogram Showing the Final Carrier (Hole) Distribution at the Break-down Field of $754 \frac{Kv}{cm}$. A Shift of Carriers into Higher Energies Can Be Seen Above.	45
5.15 Arrhenius Plot for Mobility (Log Scale) vs. Temperature.	47

Chapter 1

INTRODUCTION

Amorphous semiconductors are useful as they can mimic the properties of their crystalline counterparts while having the ability of being deposited uniformly, over a large area and at a rapid rate in a thin film geometry. This has led to the invention of the thin-film solar cell that use amorphous silicon which could be deposited over a variety of substrates. Moreover, the possibility to alloy these amorphous semiconductors provide, us with a chance to improve device performance [1]. The introduction of hydrogenated amorphous silicon increased conductivity substantially and made doping possible in amorphous materials which, in turn, allowed us to make semiconductor devices out of amorphous materials [2].

Another useful property of amorphous materials is that extremely high resistance [3]. This property is used in applications like xerography, where the amorphous material shows strong photo conductivity along with resistivity [4]. Amorphous materials are a good contender for photo-detectors in medical imaging devices as they can be deposited uniformly over large areas, this leading to larger detectors which is, in turn a requirement for larger axial field of view. A few other applications of amorphous semiconductors include memory devices [5], Ovonic switching [6], xeroradiography [7], thin-film devices [8], solar cells [9], and digital radiography.

It is important to note that the last 60 year of progress in the semiconductor industry have been largely dominated by the use of crystalline semiconductors. Crystalline materials have long range order. There are universally accepted theories, like

the band theory of carriers, which can explain the electrical properties of crystalline materials [10].

A quantum mechanical explanation for the properties of crystalline material have been based on the periodic nature of crystals and the presence of long range order. Then the motion of an electron has been described via a Bloch wave functions .

A Bloch wave function has a plane wave component that is multiplied by a cell periodic function which has the same periodicity as that of the lattice. However recent experimental studies suggest that the band theory can be extended to amorphous semiconductors, due to the retention of the crystalline co-ordination number in amorphous state. The co-ordination number in a crystal refers to the number of nearest neighbours surrounding a central atom in the complex or crystal. An electron diffraction method can be used to find the radial distribution curve which gives us the co-ordination number of a material. For example amorphous boron and germanium have a co-ordination number of 6.18 and 4.26 respectively which is comparable to the crystalline values of 6 and 4 respectively [11].

A study of one dimensional disordered chains by Gubanov [12] suggests that band gaps do exist in amorphous semiconductors leading to broadening of the electronic bands and are characterized by a disorder potential.

$$\delta E_i = \epsilon(E_1 + E_2) \tag{1.1}$$

Eq.(1.1) shows the broadening of electronic bands where E_1 and E_2 refers to the widths of the neighboring energy bands . The band gap exists as long as the forbidden gap denoted by E_g is greater than δE_i . Makinson and Roberts [13] further strength-

ens the theory by performing a numerical calculation on a disordered Kronig-Penny model. Their work states that the forbidden energy gap in a crystal structure is altered by a long range disorder existing in amorphous semiconductors, thus resulting in a finite density of states region near the edges of the allowed energy regions. These are known as localized states. It was, furthermore concluded that band structure is determined by inter-atomic distances and overlap of wave function and not by the periodic structure [14]. This shows that amorphous materials can also have a band gap depending upon a specific value of the disorder potential. Thus, there exists a growing need to study the transport mechanisms in amorphous materials. One way to study the transport properties of materials is to solve the Boltzman Transport equation.

The Boltzman transport equation is an integro-differential equation that describes the transport phenomena in semiconductors, in a semi-classical fashion (scattering is treated quantum mechanically). Though analytic solutions to the BTE [15, 16, 17] may be possible in some cases, they require drastic approximations which renders the results not as useful or inaccurate. The Monte Carlo technique was first developed in 1966 by Kurosawa [18], for the solution of the BTE. The Monte Carlo technique is a statistical numerical method [19], which is applied to the simulation of random processes and can be used to solve the low and high field properties of a semiconductor. In the long time limit the ensemble MC technique gives the solution to the BTE by giving one a direct simulation of the carrier dynamics in the material. For example as the simulation is being run, the real time physical information like the particle's energy, velocity and distribution can be extracted. Thus we can investigate properties of materials which cannot be measured using experiments and allows us to track the dynamics of every particle, throughout the simulation time. Thus while experiments

can give us results only in the macro time scale, an MC solution of the BTE can give us insight into the transport phenomena in crystalline monoclinic selenium at the picosecond time scale .

Amorphous selenium is the only amorphous material that undergoes impact ionization where only holes avalanche at high electric fields. Thus, there is a need to model high field avalanche in amorphous selenium. At high fields, the transport in amorphous selenium changes from low values of activated trap-limited drift mobility to higher values of band transport mobility, via extended states. When the transport shifts from activated mobility with high degrees of localization to extended state band transport, then the wavefunction of the amorphous material resembles that of its crystalline counterpart.

The only form of amorphous selenium used in ultra-fast radiation detectors is made by the process of Vapor-deposition. The local topology of a Vapor Deposited amorphous selenium has a predominantly ring-like symmetry, which has a distinct resemblance to the monomer ring like structure of crystalline monoclinic selenium. Thus, we model the transport of crystalline monoclinic selenium, to study the electrical properties of amorphous selenium.

1.1 Why Amorphous Selenium?

Having mentioned the various applications of amorphous materials we would now try to establish why we selected amorphous selenium (a-selenium) as our material of study. Amorphous selenium films are not only produced uniformly over a large area at a low cost, in comparison to crystalline semiconductors, but the material also

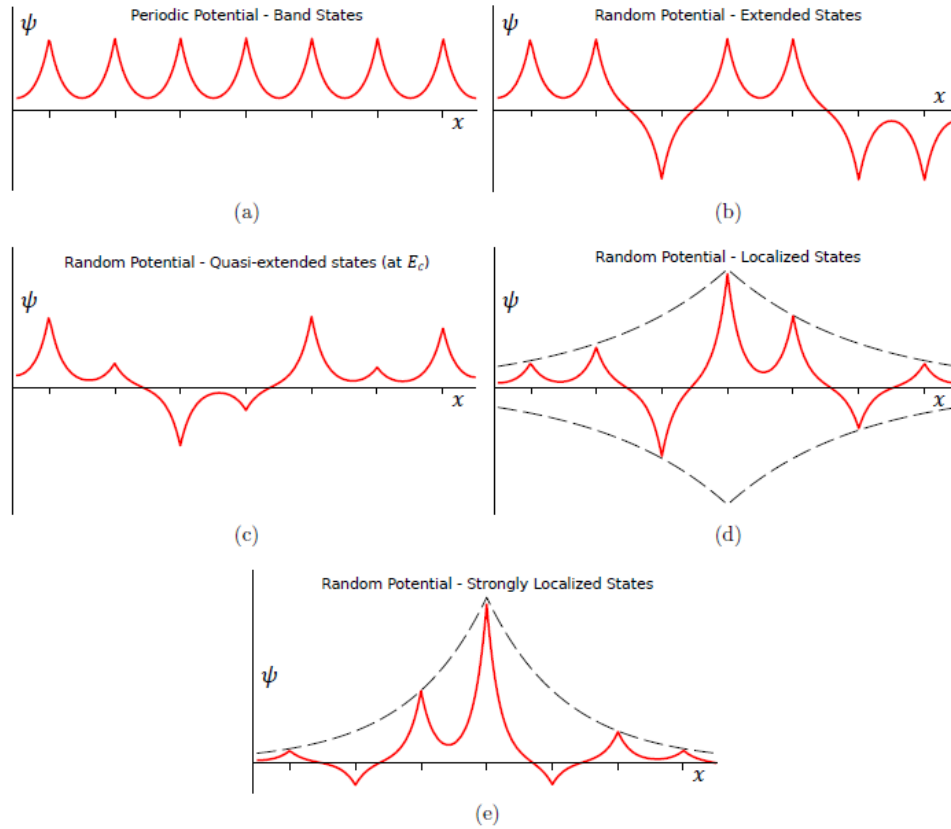


Figure 1.1: (a) Periodic Wavefunction for a Crystalline Lattice. (b) Extended Wavefunction in a Random Potential for $E > E_C$. (c) Quasi-Extended Wavefunction for $E \approx E_C$. (d) Localized Wavefunction with an Exponentially Decaying Envelope for $E < E_C$. (e) Strongly Localized Wavefunctions $E \ll E_C$.

Source: Courtesy of [20].

provides us multiple other advantages.

A-selenium melts at a relatively low temperature (*about 220°C*) compared with many other photo conductive materials, and its glass transition temperature is 40 – 50°C [21].

Thus, it can be deposited uniformly without damaging the substrate of choice and the peripheral electronics of the device. It is the only amorphous material which undergoes impact ionization gain above its critical field. Moreover, only holes avalanche in a-selenium. This is an important fact for photo detectors as it reduces the excess noise factor (ENF) which partially occurs due to the uncertainty involved in avalanche when both carriers impact ionize. Moreover a-selenium has 90% detection efficiency in the blue wavelength which makes it ideal to be coupled to a blue-emitting scintillator for high-energy radiation detection [22] . Also a-selenium is a wide band gap material with low leakage current even at high fields. When compared to crystalline silicon, a-selenium based photodetectors have the following benefits: (1) A-selenium chips are 50 times cheaper than crystalline silicon chips.(2) A-selenium photosensor shows 4 times larger the photon detection efficiency . (3) It has better signal to noise ratio in the avalanche regime [22].

Selenium based photodetectors are already being used and commercially made for direct X-ray detectors, which are deigned for full-field digital mammography (FFDM) for the best possible breast images currently available. These high-performance X-ray detectors are also suited for applications requiring high spatial resolution, such as bone imaging applications [23].

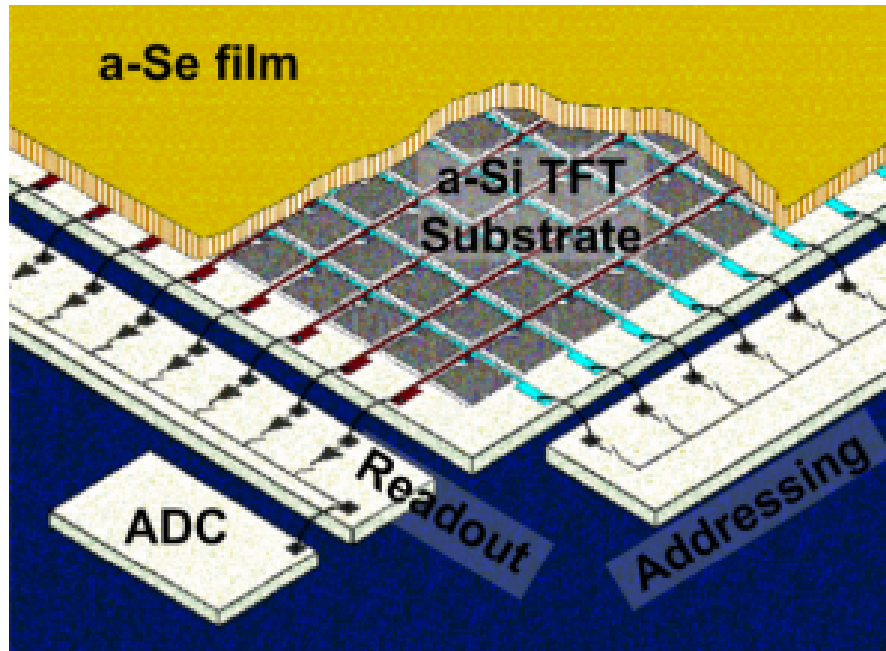


Figure 1.2: Direct Conversion Flat Panel Detector (*FPD*) for Digital Radiography Made Using A-Selenium .

Source: Courtesy of [20].

Although there exists a lot of background research on the microscopic structure of a-selenium, there is a void in knowledge when it comes to the transport mechanisms in a-selenium. This thesis tries to accomplish just that. Understanding better a-selenium material transport properties can lead to making better selenium-based devices.

1.2 Monoclinic vs Trigonal Selenium

The only form of amorphous selenium used in ultra-fast radiation detectors (used in medical imaging such as the positron emitting tomograph or in high-energy Cherenkoc imaging detector's and in time-domain spectroscopy) is made by the process of Vapor-

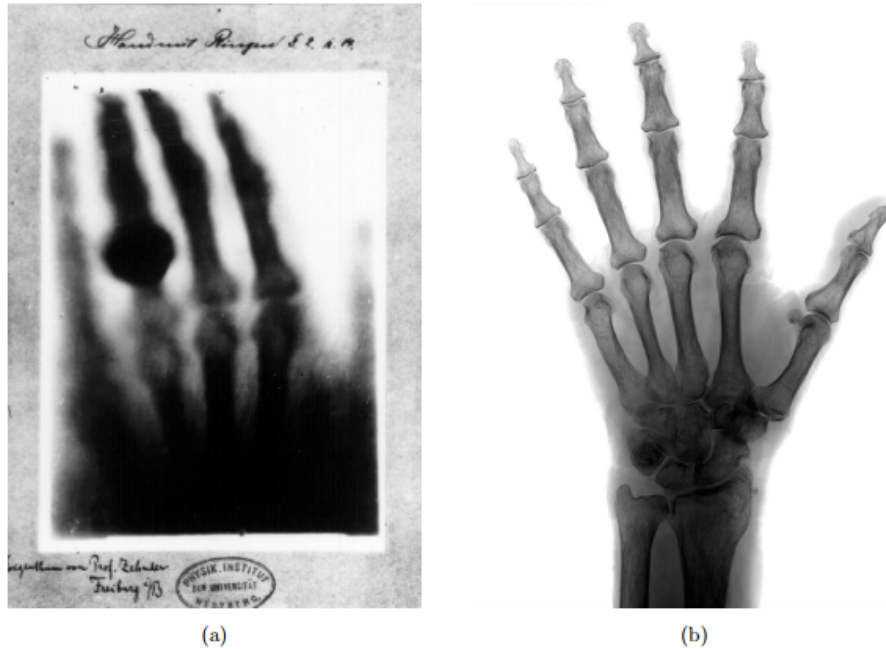


Figure 1.3: (a) The First Medical X-ray Image Taken (b) X-ray Image Taken with a Modern Day Imager .

Source: Courtesy of [20].

deposition (VD) [24]. VD is done via the condensation of thermally evaporated bulk selenium pellets onto a relatively cold substrate kept in a vacuum chamber. Most common allotropes of selenium are (1) monoclinic selenium (m-selenium) with monomer ring and (2) trigonal selenium (t-selenium) with polymeric chains. Experiments have shown that when Raman and infra-red spectroscopy was done on a-selenium , it shows resemblance of a predominantly distorted ring network . The experiments results were later confirmed by Goldan et al. [22] who performed molecular dynamic simulation on numerous VD a-selenium samples to show that they have a closer resemblance in terms of structure and bandgap of m-selenium.

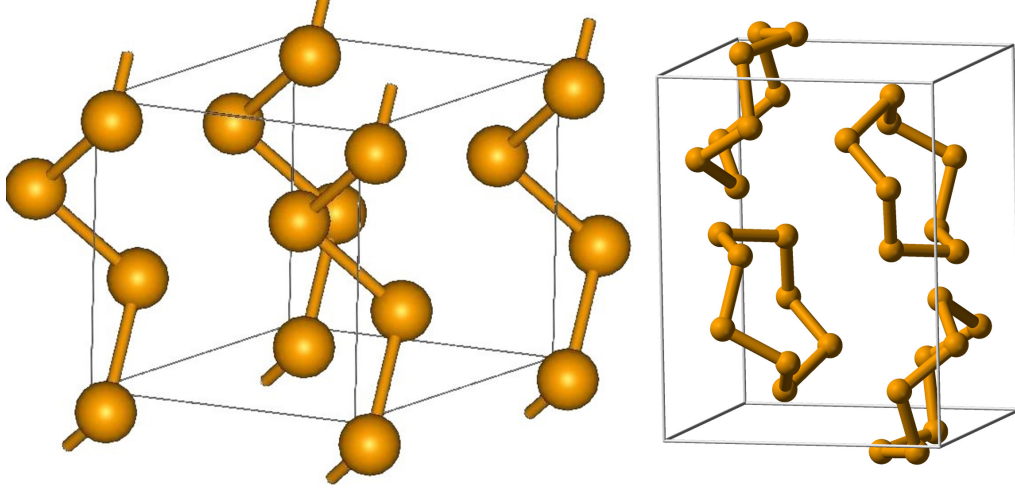


Figure 1.4: (a) Unit Cell T-selenium With Polymeric Chains Se_n . (b) Unit Cell M-selenium With Monomer Rings Se_8

Following this work we have modeled m-selenium as it has the nearest structure to that of a-selenium. Moreover, modeling a crystalline structure makes our simulations more simpler while still preserving accuracy. In addition to this numerical values of parameters like acoustic and optical deformation potential constant and effective masses can be calculated more accurately for a crystalline material. We will later come back and verify our results to experiments to prove that our choice of modeling monoclinic selenium to study the transport properties of a-selenium is indeed a correct and well thought out approach.

1.3 Organization of Thesis

The primary goal of this thesis is to calculate the mobility of m-selenium which has the same band-gap, band edge and optical properties as VD a-selenium.

In Chapter 2 we present calculation of the band structure and the density of

states function for m-selenium. Chapter 3 gives a detailed description of the relevant scattering mechanisms for m-selenium. In Chapter 4 we discuss the algorithm and various subroutines used in the bulk MC method. In Chapter 5 we present the velocity and energy field characteristics for m-selenium at various electric fields, and discuss the particle distribution at breakdown fields. We also compare the simulated mobility vs temperature results against experimental values. Our results show a relatively close match to experiments, thus validating our approach. Scope for future work and conclusions are discussed at the end of the chapter.

Chapter 2

BAND STRUCTURE AND DENSITY OF STATES CALCULATIONS USING DENSITY FUNCTIONAL THEORY

The electrical properties observed in various materials are a manifestation of variations in its energy-band diagram . In semiconductors, carriers are confined to some bands while being forbidden from other regions. Electrons are able to jump from the top of the valence band to the bottom of the conduction band by crossing an energy barrier called the "band-gap" . Nevertheless this transition requires an energy which depends on the "band-gap" and hence differs for every material. Two ways to transition from the valence to the conduction band is by absorbing either a phonon (heat) or a photon (light).

Crystalline semiconductors have a non-zero bandgap having a distinct valence and conduction band separated by a "band-gap" in which carriers cannot exist.

The absence of long range order in amorphous semiconductors leads to localized wave functions and states which exists as tails to the the allowed energy bands[25]. Localized wave functions in a disordered chain have a maximum value at some position vector x_i and decay exponentially to zero as $|x - x_i| \rightarrow \infty$ [26]. This is shown by Eq.(2.1):

$$\Psi(x) = \exp(-\beta(x - x_i)) \quad (2.1)$$

Even when these localized wave function overlap in the spacial domain , an elec-

tron cannot move from one localized state to another as both correspond to different energy values. Thus conduction at low energies is generally by hoping .

2.1 Charge Transport In Amorphous Selenium

In amorphous semiconductor the mean free path l may be lesser than the inter-atomic spacing a due to a high frequency of scattering events. As a consequence the localized bloch electron wave diminishes within the limits of a single periodic potential well. In amorphous semiconductors with strong disorder potential the electron-phonon coupling cannot be treated as a perturbation and perturbations from neighboring wells cannot be neglected.

Figure 2.1.a shows the various kinds of transport that depends on the relation between the mean free path l and the inter-atomic spacing a . The top left picture denotes a crystalline lattice where mean free path is long ($l > a$) and hence scattering is weak. The middle picture shows us Brownian motion where the mean free path is comparable to inter-atomic distance ($l \rightarrow a$). The bottom picture shows hoping conduction where scattering is very strong ($l < a$) [27].

Figure 2.1.b shows the density of states plot, showing the conduction and valence bands for regions of weak scattering when ($l > a$) dominated by band transport. The critical energies mainly E_c and E_v separate the de-localized extended states from the localized tails. This is the region where Brownian motion occurs. $E(m, e)$ and $E(m, h)$ refers to the maximum shallow state occupancy which is a product of the density of states and the thermal distribution of carriers. Here the dominant transport mechanism is hoping. Figure 2.1.b also shows a finite value for density of states which

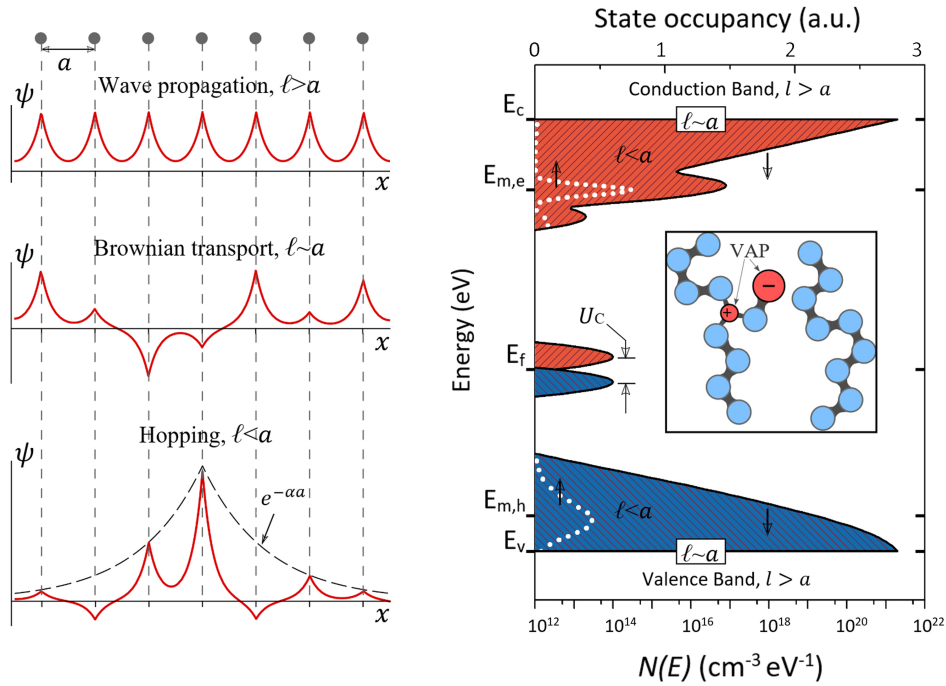


Figure 2.1: (a) Band Vs Brownian Vs Hopping Transport (b) Density of States.

Source: Courtesy of [27].

occurs due to defect centers. The defect centers occur due to the doubly coordinated neutral selenium chain with two defect sites which are oppositely charged and are called the valence-alternate pair (VAP) [28, 21, 27].

In a-selenium the carrier mobility is derived using three parallel transport mechanisms.

The first type of conduction is the diffusive Brownian motion type of transport. Here carriers travel in the extended states interrupted by frequent capture and release from shallow traps just below the critical energies E_c and E_v . This type of conduction

occurs at moderate to high temperatures . Diffusive Brownian motion can further be of two types : (1) activated trap limited mobility and (2) non activated trap limited mobility [29, 30, 27].

The second kind of conduction occurs at comparatively lower temperatures and is called Brownian motion . Here carriers can be excited to the trap sites, which have high localization, and the primary way of transport is nearest neighbour hopping between same energy levels in the tail states.

Finally at cryogenic temperatures ,occupancy is limited to a few kT 's above and below the Fermi level E_f . Now the transport method is long-range hoping or tunnelling [27] .

The conduction of holes and electrons in amorphous selenium is affected by shallow traps near the extended states as well deep trap states above and below the Fermi level. While shallow traps reduce the drift mobility of carriers travelling in the extended states, deep traps can hinder conduction entire. At moderate and even low temperature it is the shallow traps that control mobility.

Amorphous selenium suffers from the thermodynamic presence of VAP defects. Though dangling bonds are absent in amorphous semiconductors belonging to group VI of the periodic table the presence of VAP result in mid gap defect sites. In a-selenium VAP consists of a triply bonded positive Se_3^+ centre and a singly bonded positive Se_1^- . Experiments have shown that the VAP pairs cannot be removed as they are produced by thermodynamic requirements but methods such as adding impurities and alloying can help control charge transport in a-selenium. Alloying has other

advantages too. Pure α -selenium crystallizes with time and with the right ambient temperature. Adding little amounts of arsenic and chlorine and improve properties like viscosity which prevents crystallization [21].

2.2 Band Structure

We have used the Atomistix ToolKit by Quantumwise to model the band-structure of alpha-monoclinic selenium [31]. The Atomonistic Toolkit is capable of modeling the electronic properties of open and closed quantum systems within the framework of density functional theory . It uses Linear combinations of atomic orbitals (LCAO) to do this.

The key parameter in the self-consistent calculation of the Kohn–Sham equations is the density matrix, which defines the electron density. For open systems, the density matrix is calculated using non-equilibrium Green’s functions (NEGFs), while for closed or periodic systems it is calculated by diagonalization of the Kohn–Sham Hamiltonian. The electron density then sets up an effective potential, which is given by the Hartree, exchange-correlation, and external potential. Knowing the effective potential allows us to obtain the Kohn–Sham Hamiltonian.

ATK uses a numerical LCAO basis sets. The accuracy depends on the number of orbitals and the range of the orbitals. Increasing the number of orbitals and their range decrease the efficiency and increase the memory requirement. We have used a basis set called the SG15 [32] which systematically improve the accuracy. For the other pseudo-potentials the improvement in accuracy is less systematic.

Figure 2.2 shows the .cif file that we used for the band-structure calculation . The

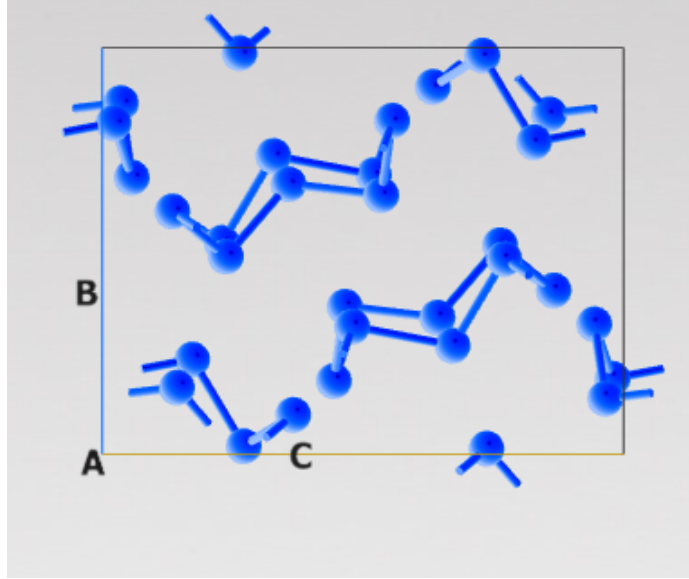


Figure 2.2: Crystallographic File for Alpha M-selenium Showing Se_8 Rings.

k-sampling used in this calculation is 5. Figure 2.3.a shows the bandstructure for alpha monoclinic selenium with Figure 2.3.b showing band gap of monoclinic selenium which has a value of 2.126 eV and is a direct in nature as the maximum and minimum values of the valence and conduction band occurs at the Gamma point.

2.3 Density of states Calculations

Once we have the Bandstructure we can generate the DOS for the conduction and valence bands. The DOS is used in the calculating of the phonon scattering rates.

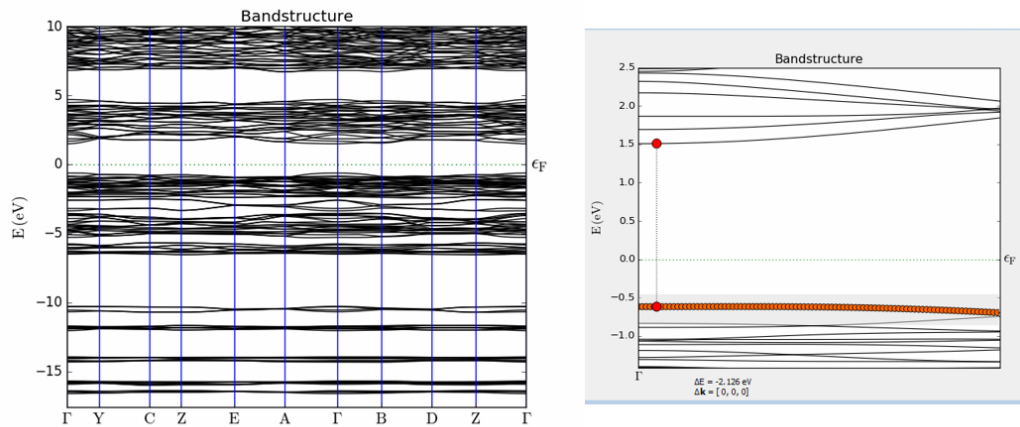


Figure 2.3: (a) Band-structure of Alpha M-selenium (b) Direct Band-gap Showing a Value of 2.126 eV.

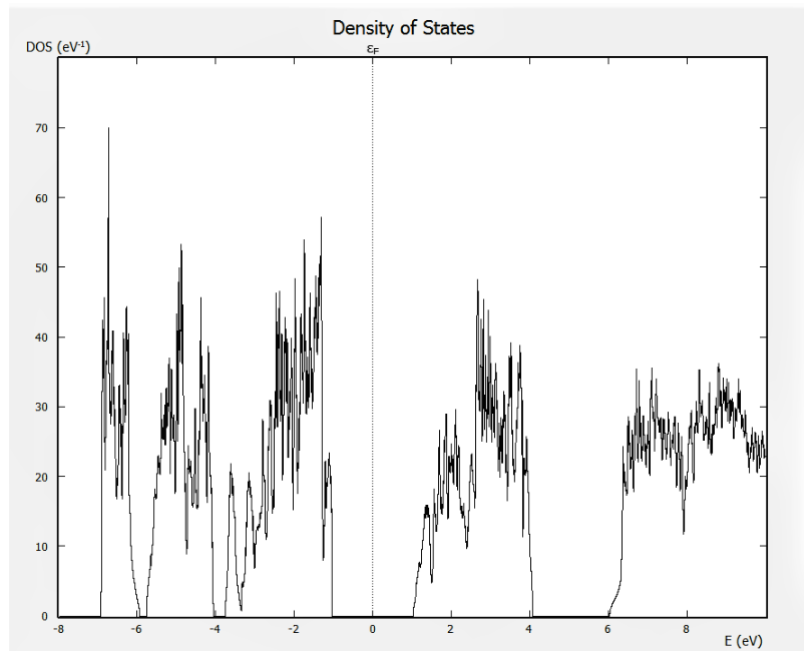


Figure 2.4: Density of States for M-Selenium

Chapter 3

SCATTERING MECHANISMS IN MONOCLINIC SELENIUM

In this chapter we will first talk about the scattering mechanisms that are relevant to m-selenium. In chapter 2 we have established the importance of electron-phonon scattering due to the trapping and release effects associated with the localized states, just above the extended states in the valence band. Optical phonon scattering has long been considered as the primary scattering mechanisms for amorphous materials. Later Fischetti et al.[33, 34] emphasized the importance of incorporating acoustic phonon scattering mechanisms into their MC calculations so as to accurately model velocity runaway effects at breakdown fields.

In our work we primarily consider acoustic and non-polar optical phonon scattering mechanisms. We have generated a DOS function from the bandstructure of m-selenium and thus are not concerned with the inter-band scattering mechanisms. Since we model crystalline monoclinic selenium, to study the transport of amorphous selenium, we have not considered the deep level traps occurring due to the VAP defects (VAP defects are common in amorphous semiconductors and are not found in crystalline ones). This reduces the complexity and can be considered as a first order approximation to understand the transport in a-selenium. Moreover we are only concerned with hole transport as it is a well established fact that only holes become hot carriers in amorphous selenium while electrons transport via hopping.

To start with, we have a DOS function calculated from the Atomistic simulations using Quantumwise tool.

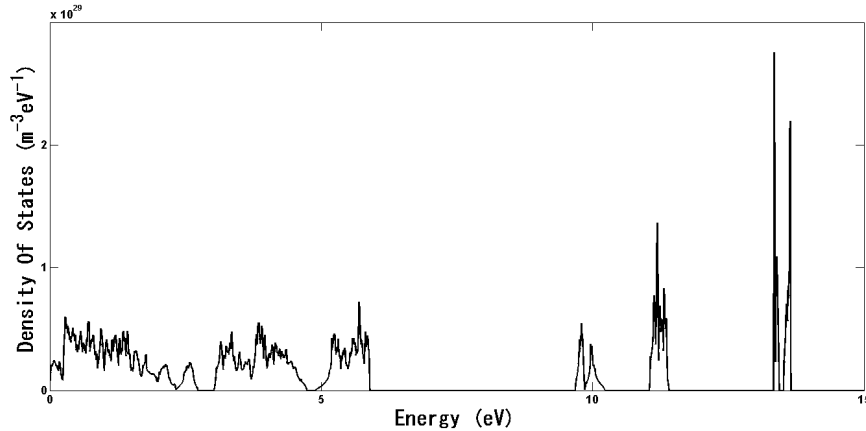


Figure 3.1: Valence Band Dos for M-selenium. 0 In the Energy Axis Refers to the Top of the Valence Band.

3.1 Fermi's Golden Rule

In the Bulk MC Technique, the carrier free flight is interrupted by memory-less scattering processes which are calculated quantum mechanically. It is here that we invoke Fermi's Golden rule.

Thus, the calculation of total scattering rates out of state k requires a definition of scattering potential for every mechanism. Eq.(3.1) states that every mechanism leads to a different "matrix element" which depends on the initial and final wave vectors along with their respective energies and the perturbation H .

$$M(k, k') = \langle \psi_{k',q} | H | \psi_{k,q} \rangle \quad (3.1)$$

Eq.(3.2) states the Fermi's Golden Rule which is a result of solving the time-dependent Schrödinger equation using first-order perturbation theory. It gives the probability of transition to a state k' in band n' from state k in band n . In the equation below E_k and $E_{k'}$ are the corresponding kinetic energies and $\hbar\omega_q$ is the

phonon energy and $\delta(E_{k'} - E_k \pm \hbar\omega_q)$ describes the conservation of energy during the scattering process.

The energy conserving delta function is only valid in the long-time limit which can be invoked when the scattering events are infrequent. In Eq.(3.2) the top sign denotes phonon emission while the bottom sign denotes absorption.

$$P(k, k') = \frac{2\pi}{\hbar} |M(k, k')|^2 \delta(E_{k'} - E_k \pm \hbar\omega_q) \quad (3.2)$$

Summation of the above equation over the entire final state give us the total scattering rate out of state k and energy E_k :

$$\Gamma(k) = \frac{1}{\tau(k)} = \frac{2\pi}{\hbar} \sum_{k'} |M(k, k')|^2 \delta(E_{k'} - E_k \pm \hbar\omega_q) \quad (3.3)$$

Below, we derive the matrix element squared for acoustic and non-polar optical phonon scattering.

3.2 Acoustic Scattering

Acoustic scattering occurs due to the strain tensor when lattice atoms start vibrating in the same direction. This causes a deformation of the unit cell and the differential displacement along with the deformation potential forms the perturbation potential for acoustic phonon scattering [35]. Acoustic phonon scattering can be interband or intraband.

Figure 4.2 shows an isotropic elastic substance of length Δx subject to a strain tensor such that the element extends from x to $x + \Delta x$. In the presence of a strain (which is the acoustic lattice vibrations) the left side is extended by a length of U_x and the right side by a length of $U_x + \Delta x$. The derivative of the change in length is denoted as ϵ_{xx}

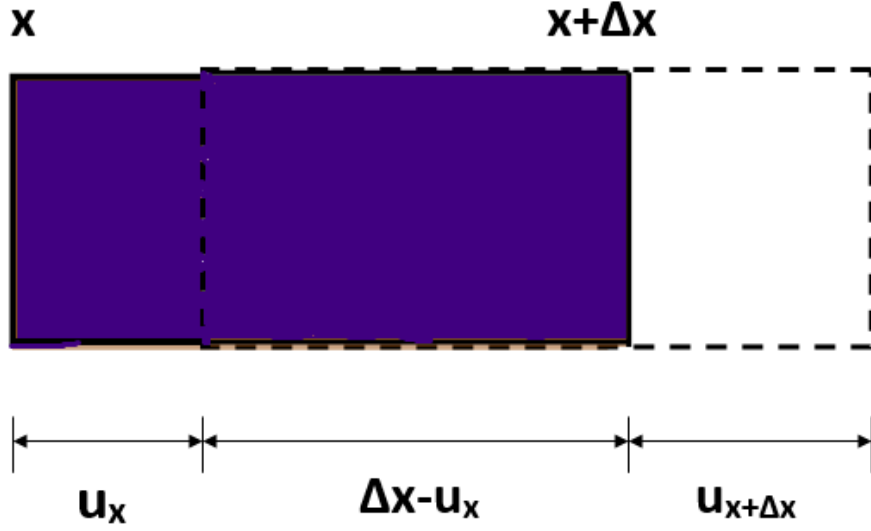


Figure 3.2: Fractional Change in Length Due to Strain Tensor

$$\frac{du_x}{dx} = S(x) = \epsilon_{xx} \quad (3.4)$$

The increased length, denoted by $\Delta x'$ leads to differential change in volume as a result of this deformation.

$$\Delta x' = \Delta x + \epsilon_{xx} \Delta x = (1 + \epsilon_{xx}) \Delta x \quad (3.5)$$

$$\frac{\delta V}{V} = \epsilon_{xx} + \epsilon_{yy} + \epsilon_{zz} = \Delta \cdot u = \nabla \quad (3.6)$$

Note ∇ is expressed in terms of phonon creation a_{qv}^+ and phonon annihilation a_{qv}^- operators:

$$\nabla = \Delta \cdot u = \sum_{q,v} \sqrt{\frac{\hbar}{2mN\omega_{qv}}} \vec{q} \vec{e}_q [a_{\vec{q},v}^- e^{i\vec{q}\vec{r}} - a_{\vec{q},v}^+ e^{-i\vec{q}\vec{r}}] \quad (3.7)$$

Then, the Hamiltonian for the hole-phonon interaction is given by Eq.(3.8) where Ξ_{ac} is the acoustic deformation potential tensor.

$$H_{hp} = c\nabla = \Xi_{ac}\Delta.u \quad (3.8)$$

The matrix element for acoustic phonon scattering is then calculated using:

$$M_{ft} = \sum_{q,v} \langle \Psi_f | u_{qv}(R,t) H_{qv}(r) | \Psi_i \rangle \quad (3.9)$$

Where Ψ_f and Ψ_i are the initial and final wavefunctions.

Once the integration is completed across phonon variables, the final matrix element, ignoring non parabolicity is given by:

$$M(k, k')^2 = \frac{\hbar \Xi_{ac}^2}{2\rho V \omega_q} q^2 (n_q + \frac{1}{2} \pm \frac{1}{2}) \delta(\vec{k}' - \vec{k} \pm \vec{q}) \quad (3.10)$$

In Eq.(3.11) n_q is the phonon number density given by the Bose-Einstein distribution function:

$$n_q = \frac{1}{e^{\frac{\hbar \omega_q}{k_B T}} - 1} \quad (3.11)$$

Intraband acoustic phonon scattering involves phonons with energy that is approximately 1 meV while the thermal energy at room temperature is 38 meV. Thus, the scattering can be considered as elastic ($\hbar \omega_q < k_B T$). Thus, in addition to the interactions with electrons being elastic, it also leads to the matrix elements for absorption and emission to be the same ($n_q \equiv n_q + 1$). This is known as equipartition approximation.

Then, within the equipartition approximation,

$$n_q = \frac{1}{e^{\frac{\hbar\omega_q}{k_B T}} - 1} \gg 1 \quad \text{for } \hbar\omega_q \ll k_B T \quad (3.12)$$

Hence, in the elastic and equipartition approximation, the matrix element finally reduces to.

$$M(k, k')^2 = \frac{\Xi_{ac}^2 k_B T}{2\rho V V_s^2} \quad (3.13)$$

Then, the total scattering rate out of state k is:

$$\frac{1}{\tau(k)} = 2 \frac{mV}{2\pi \hbar^3 k} \int_0^{2k} q M(k, k')^2 dq \quad (3.14)$$

which leads to :

$$\frac{1}{\tau(k)} = \frac{2\pi}{\hbar} \frac{\Xi_{ac}^2 k_B T}{2\rho V_s^2} \frac{1}{2} g_c(E_k) \quad (3.15)$$

In Eq.(3.15) $g_c(E_k)$ is the energy dependent DOS , ρ is the density ($4500 \frac{kg}{m^3}$) and V_s is the speed of sound in m-selenium which is $1750 \frac{m}{s}$.

The acoustic deformation potential was taken from literature [36] and tabulated against energy and used as a energy dependent file. Figure 3.3 shows the plot for the deformation potential Ξ_{ac} . The scattering rate vs. Energy for m-selenium is shown in Figure 3.4

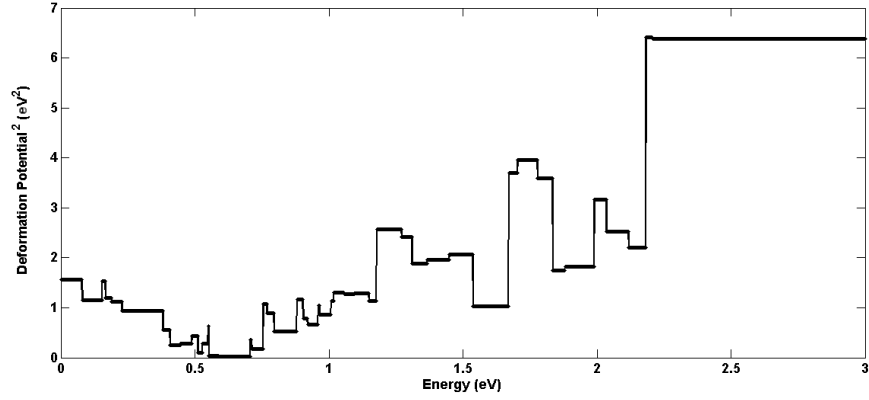


Figure 3.3: Deformation Potential Squared vs. Energy

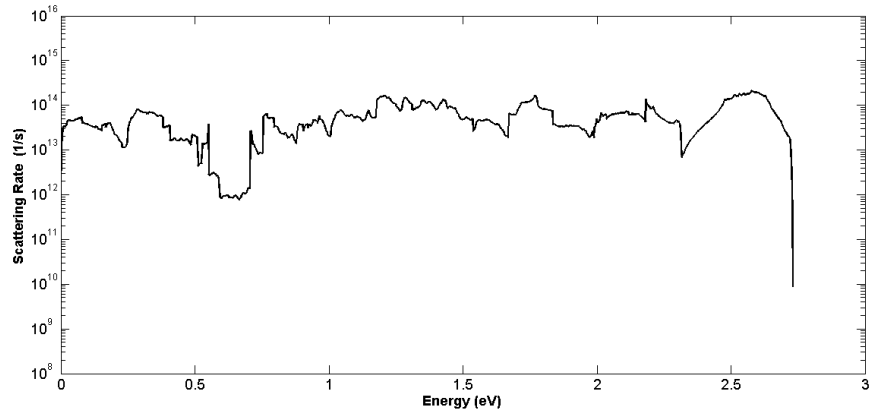


Figure 3.4: Acoustic Scattering Rate (Log Scale) vs. Energy.

3.3 Non-polar Optical scattering

Optical phonon scattering occurs due to the out of phase motion of the lattice atoms . The Hamiltonian describing the electron-phonon interaction is shown in eq.(3.16). Unlike the case of acoustic scattering, the long wavelength optical displacement is no longer a slowly varying function and effects the Hamiltonian directly. \vec{D}_o represents the optical deformation potential while \vec{u} represents the relative displacement of the atoms in the unit cell. Then:

$$H_{hp} = \vec{D}_o \cdot \vec{u} \quad (3.16)$$

The matrix element then takes the form :

$$M(k, k')^2 = \frac{\hbar \vec{D}_o^2}{2\rho V \omega_{qv}} \left(n_{qv} + \frac{1}{2} \pm \frac{1}{2} \right) \delta(\vec{k}' - \vec{k} \pm \vec{q}) \quad (3.17)$$

Since we are concerned with intraband scattering, which is affected by the long wavelength phonons at the centre of the Brillion zone where the dispersion curve for optical phonons is flat, ($\omega_{qv} = \omega_o = const$). The $\pm \frac{1}{2}$ refers to the emission and absorption processes respectively.

In general, we have to use the following expression for the total scattering rate out of state k:

$$\frac{1}{\tau(k)} = \frac{mV}{2\pi \hbar^3 k} \left(\int_{q_{min}^{ab}}^{q_{max}^{ab}} q M(k, k')^2 dq + \int_{q_{min}^{em}}^{q_{max}^{em}} q M(k, k')^2 dq \right) \quad (3.18)$$

Since the matrix element is independent of the phonon wave vector it can be taken out of the integration . This means that the scattering process is isotropic. The limits to the absorption and emission processes are calculated by equating the energy conserving delta function to zero.

The phonon energies involved in the scattering process is between 20 *meV* and 60 *meV* which is comparable to the thermal energy at room temperature and thus the scattering process is inelastic in nature. Only for some very energetic phonons can the scattering process be considered as elastic.

Thus the final scattering rate takes the form :

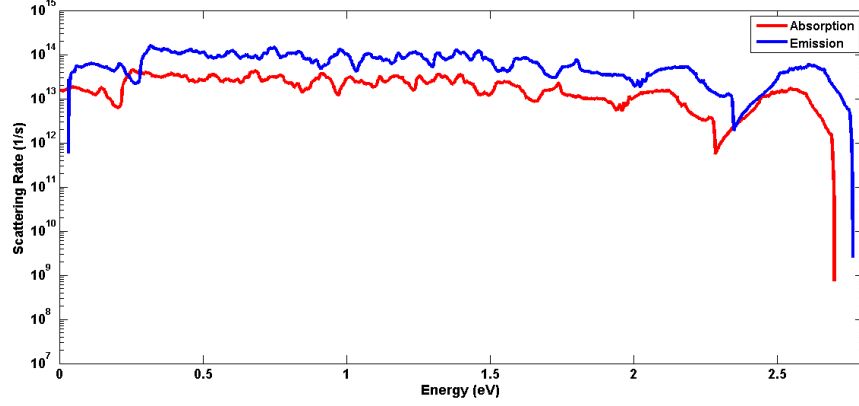


Figure 3.5: Non-polar Optical Scattering Rate (Log Scale) vs. Energy .

$$\frac{1}{\tau(k)} = \frac{m^{\frac{3}{2}} \vec{D}_o^2}{\sqrt{2} \pi \hbar^3 \rho \omega_o} [(n_0) \sqrt{E_k + \hbar \omega_o} + (n_0 + 1) \sqrt{E_k - \hbar \omega_o}] \quad (3.19)$$

Now since we have a energy dependent DOS function , we substitute the expression for a 3-D DOS into Eq.(3.19) to get the result given in Eq.(3.21) . G_c refers to the 3-D Dos in Eq.(3.20)

$$g_c = \frac{m^{\frac{3}{2}} \sqrt{E_k} \sqrt{2}}{\pi^2 \hbar^3} \quad (3.20)$$

$$\frac{1}{\tau(k)} = \frac{\pi \vec{D}_o^2}{\rho \omega_o} [(n_0) \frac{1}{2} g_c + (n_0 + 1) \frac{1}{2} g_c] \quad (3.21)$$

In eq.(3.22) ρ is the density of m-selenium ($4500 \frac{kg}{m^{-3}}$) and the phonon energy was calculated from the DFT phonon bandstructure calculation to be $32 meV$. The optical deformation potential constant \vec{D}_o has a value of $4 * 10^{10} \frac{eV}{m}$

BULK MONTE CARLO THEORY

The BTE under the semi-classical approximation, is used to predict the electrical behaviour of a semiconductor material. It is a complex integro-differential equation in seven dimensional space, three in momentum space, three in real space and one in time. Consider a phase space around the point (x, y, z, p_x, p_y, p_z) . If $f(x, y, z, p_x, p_y, p_z)$ represents the distribution function, which denotes the probability of finding a particle in that phase space, then the change in the distribution function df , that occurs in time interval dt , due to the movement of particles in real space and due to the fact that force fields move the particles from one momentum space to another is shown in Eq.(4.1) [37].

$$\frac{df}{dt} = -v \cdot \nabla_r f - F \cdot \nabla_p f \quad (4.1)$$

Particles may also be transferred in and out of the phase space by scattering interactions, which may involve other particles of the distribution or scattering centers external to the assembly of the particles under consideration [38].

$$\frac{df}{dt} = -v \cdot \nabla_r f - F \cdot \nabla_p f + \left. \frac{df}{dt} \right|_{coll} + s(r, p, t) \quad (4.2)$$

In Eq.(4.2) the first term in the right denotes the diffusion processes which may occur due to temperature or concentration gradients. The second term on the right describes the drift processes due to gradients existing as a result of electrical and magnetic fields. The third term denotes the collision integral which is difference between

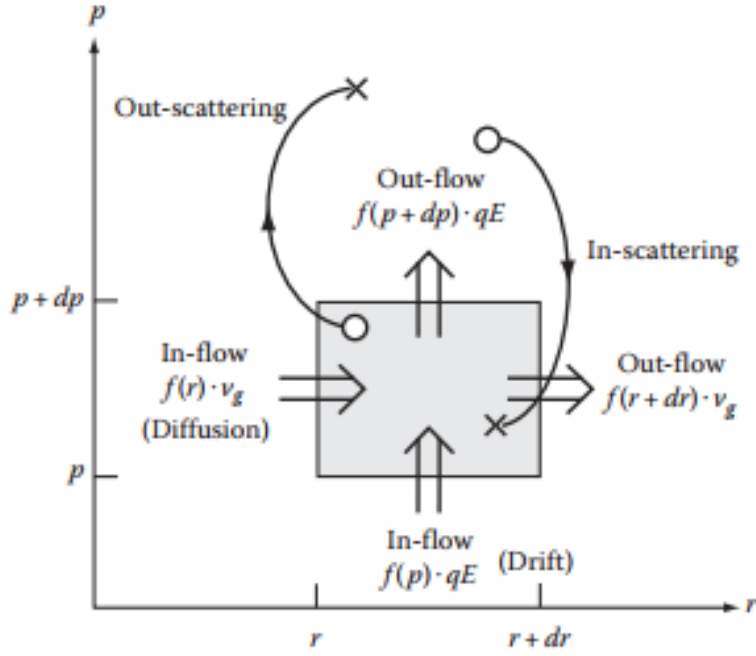


Figure 4.1: Shows Three Dimensional Processes Namely Drift Diffusion and Collision in Two Dimensional Space.

the in and out of state scattering processes involved in changing the distribution function. The last term denotes the generation and recombination processes which can be modeled using a kinetic MC technique and is left out of this work.

$$\frac{df}{dt}|_{coll} = \sum_{k'} (S(k', k)f(k')(1 - f(k)) - S(k, k')f(k)(1 - f(k'))) \quad (4.3)$$

Eq.(4.3) describes the collision integral. The first term inside the summation represents in scattering where $S(k', k)$ denotes the probability of scattering from state k' to state k . In Eq.(4.3) $f(k')$ represents the probability of state k' being filled and $(1 - f(k))$ represents the probability of the state $f(k)$ being empty. Similarly the second term in the right of Eq.(4.3) denotes out scattering.

The MC method is a stochastic method used to solve the BTE. Below we describe the various subroutine in the MC algorithm for the solution of the BTE (In the long time limit).

4.1 Bulk Monte Carlo Algorithm

The MC technique allows us to model the transport of carriers in a semiconductor and thus monitor and optimize its electrical properties. The bulk MC theory considers an ensemble of particles which are accelerated in the direction of an electric field by a mechanism called free flight and their trajectory is interrupted by instantaneous scattering events. The scattering interactions decide the final energy and momentum of the particles. At the end of a sufficiently long simulation time (long enough for the energy to saturate), ensemble parameters like velocity and energy can be calculated for a specific electric field. Running the same simulation for a wide range of electric fields , gives us the mobility . If we go a step further and repeat the process for a range of temperatures then the electrical properties against temperatures can be plotted. The bulk MC algorithm is shown in Figure 4.2.

4.2 Parameters Initialization

In this subroutine we define all the constants that we need while writing the bulk MC code. Values defined here will remain constant throughout the course of the simulation.

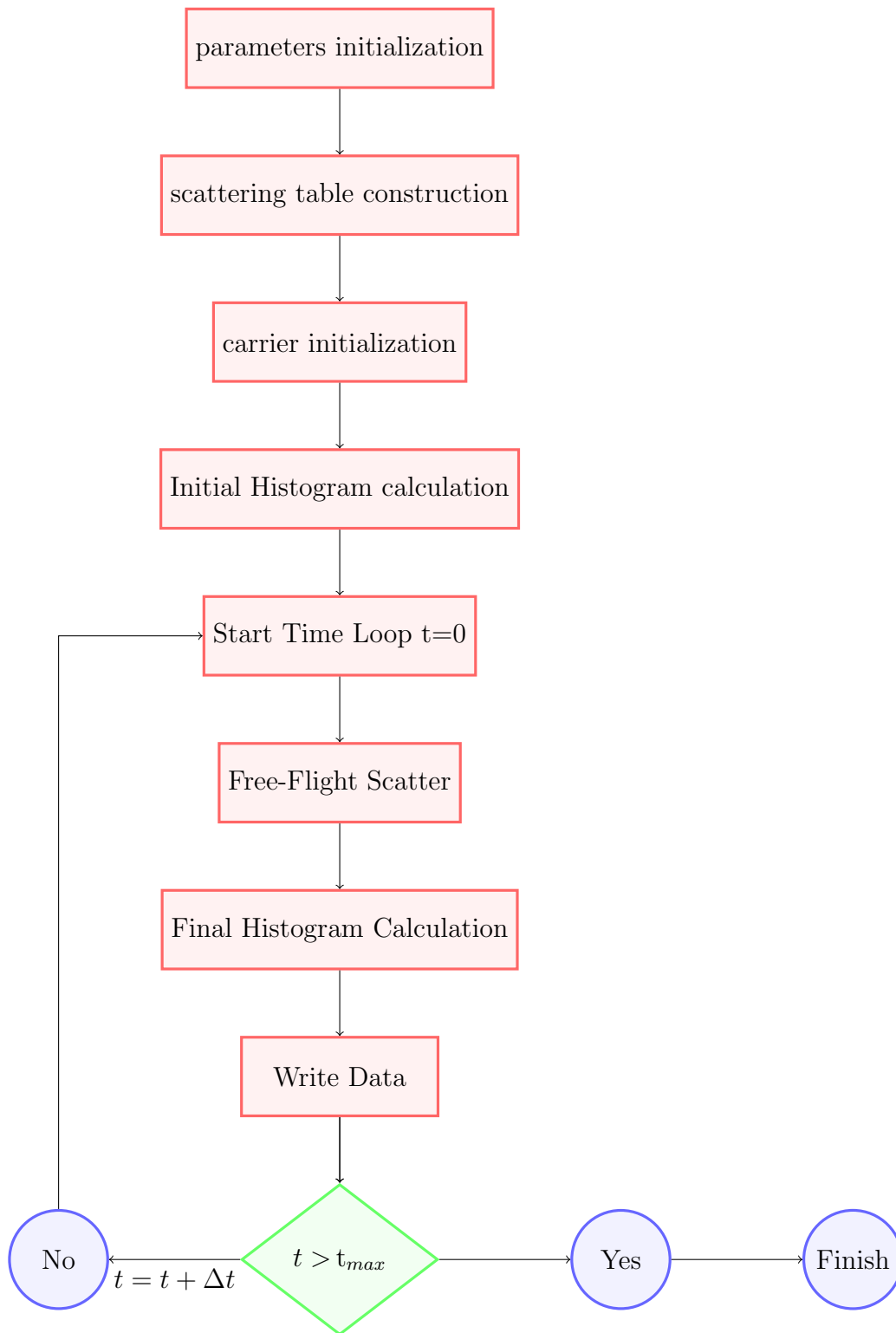


Figure 4.2: Bulk Monte Carlo Algorithm

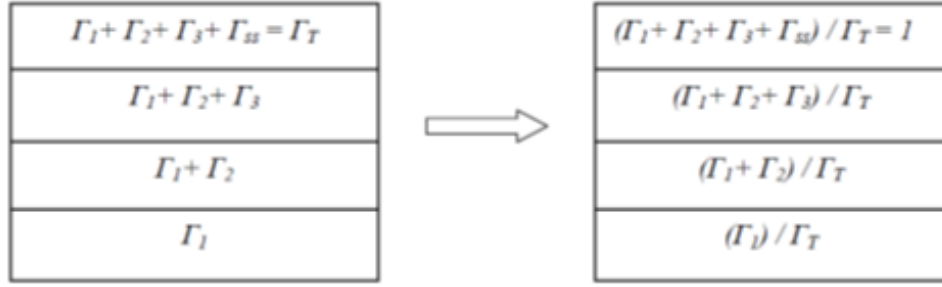


Figure 4.3: Scattering Table Creation.

4.3 Scattering Table Construction

Having derived the scattering rates for acoustic and non polar optical phonon scattering, we next calculate the cumulative rates and the maximum scattering rate Γ_{max} . We do this by adding up all the individual scattering rates and the self-scattering [39], as shown in Eq.(4.4). In Eq.(4.4) n denotes the total number of scattering mechanisms. The advantage of self scattering is that it does not change the energy or momentum of the carriers and adjusts itself in time so that the total scattering rate is a constant.

$$\Gamma_{total}(E) = \sum_{i=1}^n \Gamma_i(E) + \Gamma_{self-scatter}(E) \quad (4.4)$$

Next we go on and find the energy at which the scattering rate is the maximum Γ_{max} and then divide the whole table by the maximum value Γ_{max} . This is called normalization of the scattering table which makes the range of values for the scattering rates between 0 and 1, and the selection of scattering mechanism is determined by drawing a random number uniformly distributed between 0 and 1.

4.4 Carrier Initialization

It is here that we define the initial wave vectors k_x , k_y , k_z and the energy E of the carriers. The total number of carriers is taken to be 50,000 and the carrier energy is initiated to $\frac{3}{2}K_B T$ multiplied by the *log* of a random number between 0 and 1 . Thus the initial energy distribution has Maxwell-Boltzmann form.

4.5 Histogram Calculation

Histograms are calculated twice during the Monte Carlo simulation flow. Initially we calculate the histograms to plot the initial distribution of the carriers. This subroutine is only called once in the entire program. The histogram subroutine is called a second time after each time step when we again store and calculate parameters such as velocity , energy and valley occupancy of the particles.

To obtain the time evolution of the particles , the simulation is divided into time-steps of Δt length and the ensemble averages are taken at every time step.

The velocity in the x , y or z direction for a single particle is calculated as follows:

$$v_{x,y,z}(t) = \frac{\hbar_{x,y,z}(t)k_{x,y,z}(t)}{m} \quad (4.5)$$

Next , we add the velocities and energies for all the particles and then divided the cumulative sum by the total number of particles. This gives the average velocity and average energy at a particular time-step. Hence :

$$v_{average} = \frac{1}{N} \sum_{i=1}^N v_{sum}(t) \quad (4.6)$$

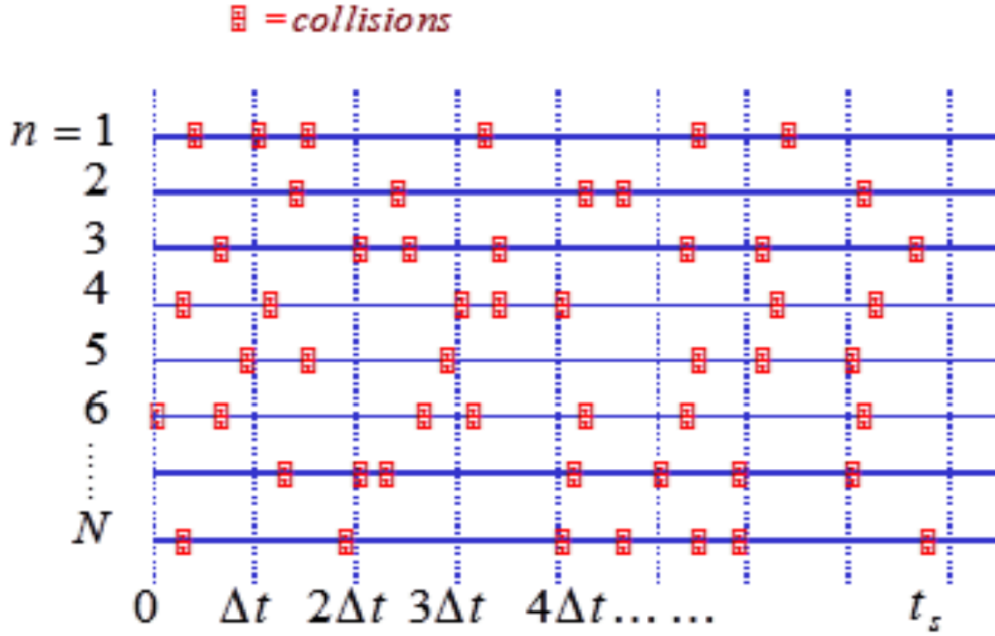


Figure 4.4: Free-Flight Scatter Representation of the Monte Carlo Method.

Source: Courtesy of [38].

$$E_{average} = \frac{1}{N} \sum_{i=1}^N E_{sum}(t) \quad (4.7)$$

Where N is the number of particles in the ensemble.

4.6 Free-Flight Scatter Subroutine

Once the time loop starts this subroutine is called after every sampling time Δt . At first every carrier is drifted using the drift subroutine, as per the applied electric field.

The free flight time is calculated as follows:

$$tc = -\log(rr) \frac{1}{\Gamma_{max}} \quad (4.8)$$

Where rr represents a random number and Γ_{max} refers to the maximum scattering rate value.

The change in wave vector δk and the carrier's new energy is calculated as shows in Eq.(4.8) where F refers to the applied electric field:

$$\delta k = -\frac{qF}{\hbar} tc \quad (4.9)$$

The new wave vector and energy is calculated using:

$$k_{new} = k_{old} + \delta k, \quad (4.10)$$

$$E_{new} = \frac{\hbar^2 k_{new}^2}{2m}. \quad (4.11)$$

After a carrier undergoes free flight , under the drift subroutine , the changes in momentum result in change in energy. Next a suitable scattering mechanism is selected based on this energy and a random number (between 0 and 1) is generated. If the random number falls between mechanism i and mechanism $i + 1$, then mechanism $i + 1$ is selected. The final state of the particle is then calculated by changing the carrier's wave vector and energy , depending on the type of scattering which the particle underwent.

The change in angle and energy is done using a subroutine called scatter-carrier.

The scatter-carrier subroutine is called at the end of the drift process. If the scattering process is elastic, the energy before and after scattering remains the same. For

the interaction between carriers and the vibrational modes of the lattice described as quasi-particles known as phonons, electrons exchange finite amounts of energy with the lattice in terms of emission and absorption of phonons [38] . This is called in-elastic type of scattering. In this work acoustic phonon scattering is considered as elastic under the elastic and equipartition approximation, whereas the non-polar optical phonon scattering is in-elastic in nature.

The angle after scattering depends on the scattering mechanism being isotropic or an-isotropic . An isotropic scattering mechanism (both acoustic and non polar optical scattering in our case) favors scattering in all directions equally and thus the direction of the wavevector is randomized . The magnitude of the wavevector k is then calculated from the new energy value using the parabolic E-k relationship. Figure 4.5 illustrates the complete free flight scatter subroutine.

In the next chapter we will present the results of our simulation.

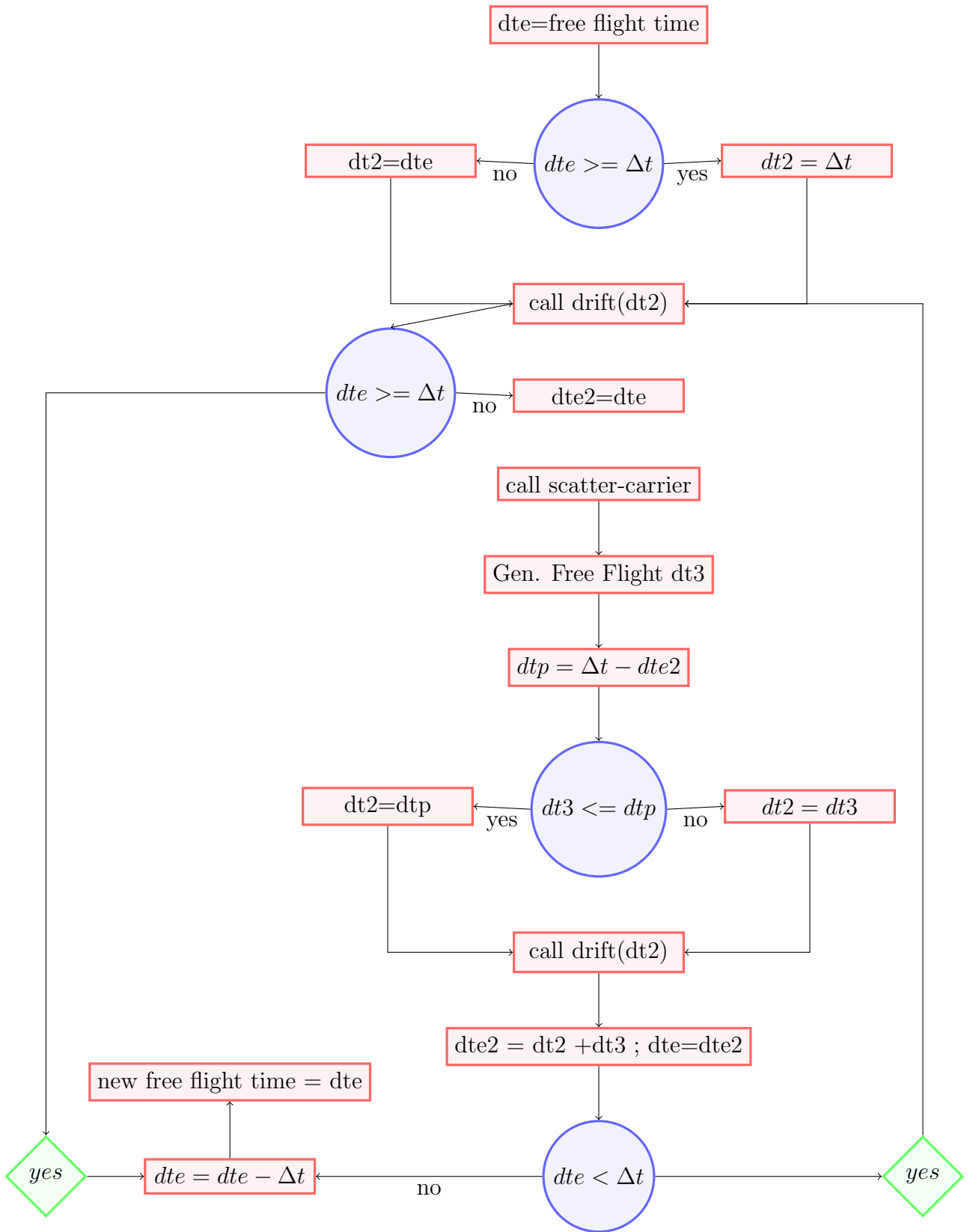


Figure 4.5: Free-Flight Scatter Subroutine in One Flowchart

Chapter 5

RESULTS AND CONCLUSIONS

The bulk MC code was used to reproduce the experimental results of m-selenium and to test its transport properties . We have used a single fitting parameters, to best fit the simulated results to the experimental data. The fitting parameter used in this work is the hole effective mass which was assumed to be 3.68 times the rest mass of a hole. This is not far from realistic values, as the atomistic simulations done for m-selenium in the QuantumWise tool produced an effective mass, equal to 3.5 times the rest mass of a hole.

Table 5.1: Bulk Monte Carlo Parameters

Parameter	Value
Total Sim. Time	20 Picoseconds
Time Increment	0.05 Picoseconds
Number of particles	50,000
Effective Mass (Holes)	3.68
Electric Field Range	1-1000 kV/cm

5.1 Initial Histograms

Here we present the results for the carrier (energy and wave vector) distributions at $t=0$. The total number of particles considered for the MC code is 50000.

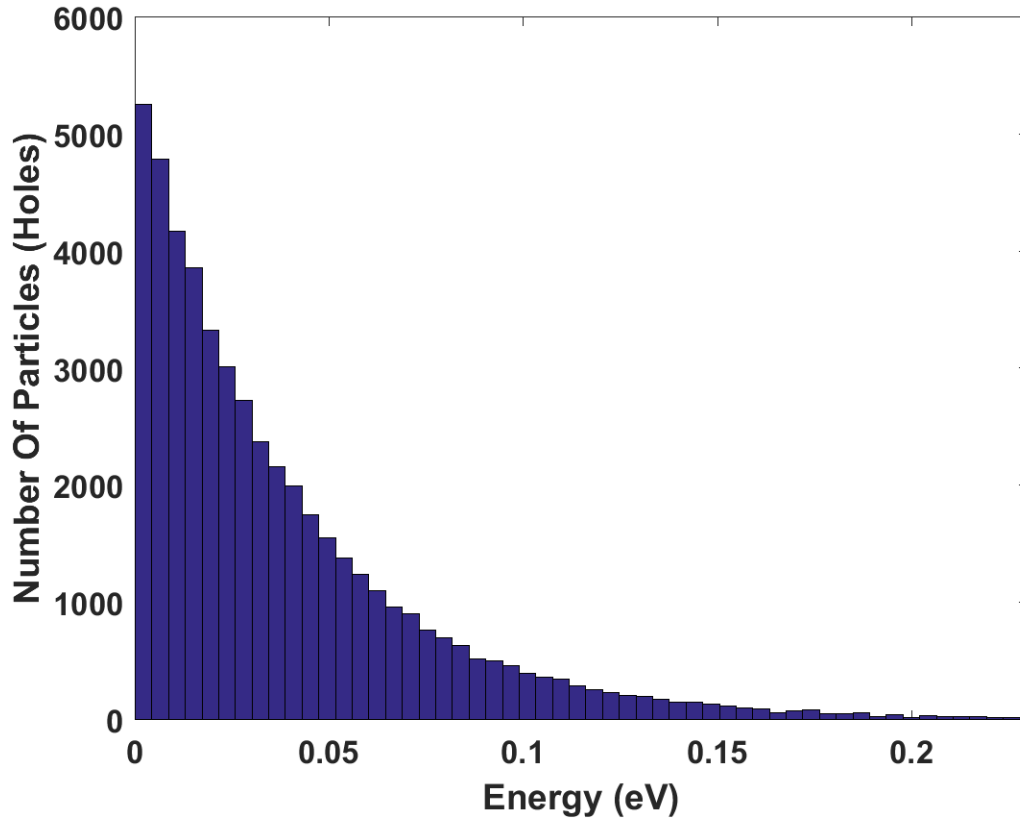


Figure 5.1: Histogram Showing the Initial Carrier Energy Distribution.

Figure 5.1 shows the histogram for the initial carrier energy distribution. The average initial energy was calculated from this histogram to be 38.6 meV, which is the thermal energy at room temperature. Each bin in the histogram is 4meV. It has the Maxwell-Boltzmann form as expected.

The next three figures, namely Figures 5.2 , 5.3 and 5.4 shows the histograms for the initial carrier wave vector distribution in the k_x , k_y and k_z directions respectively. The initial wave vector components are symmetric around the y-axis of the plot, which means that the average wavevectors are zero(which should be expected since the electric field is zero at $t = 0$).

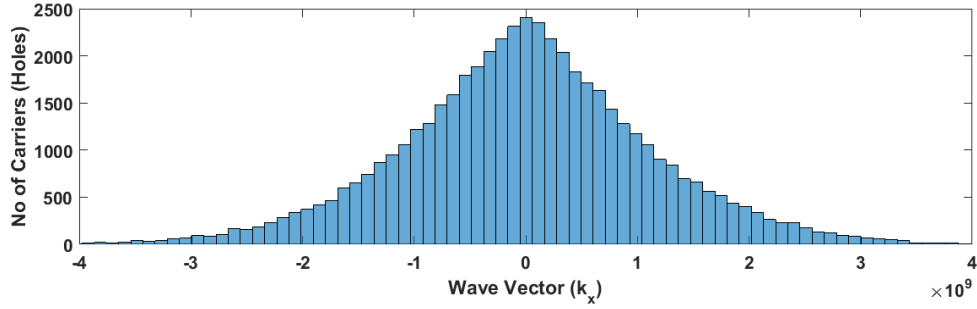


Figure 5.2: Histogram Showing the Initial Carrier Wave Vector (k_x [1/m]) Distribution.

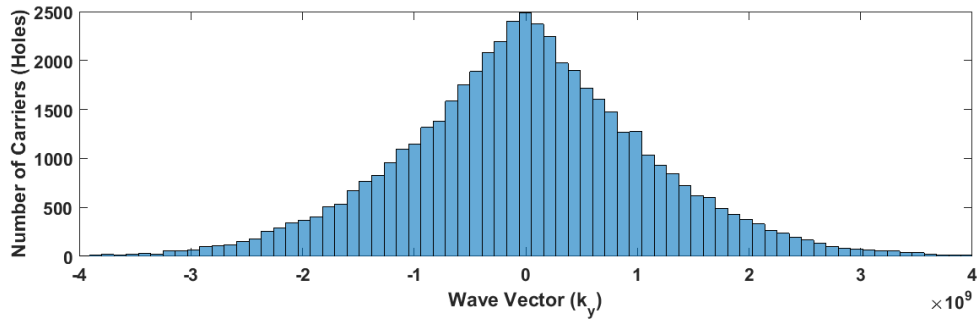


Figure 5.3: Histogram Showing the Initial Carrier Wave Vector (k_y [1/m]) Distribution.

5.2 Final Histograms

In this section, we will discuss the carrier distributions at the end of the simulation time domain (20 picoseconds). The electric fields used here is $50 \frac{kV}{cm}$. The electric field is applied along the x-axis.

The histogram for the final carrier energy distribution has a drifted Maxwellian form due to the applied electric field.

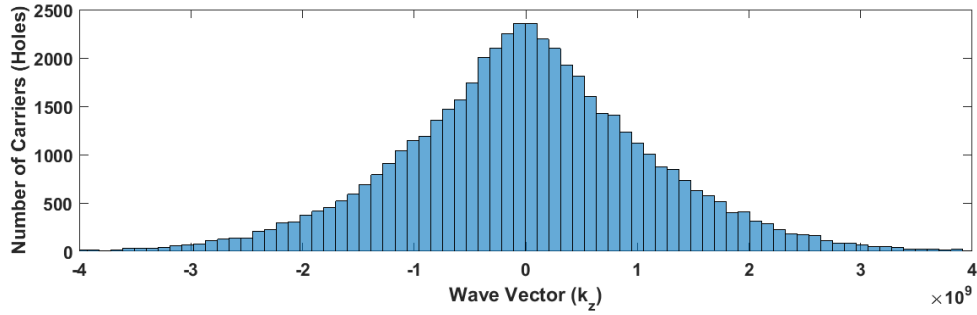


Figure 5.4: Histogram Showing the Initial Carrier Wave Vector (k_z [1/m]) Distribution.

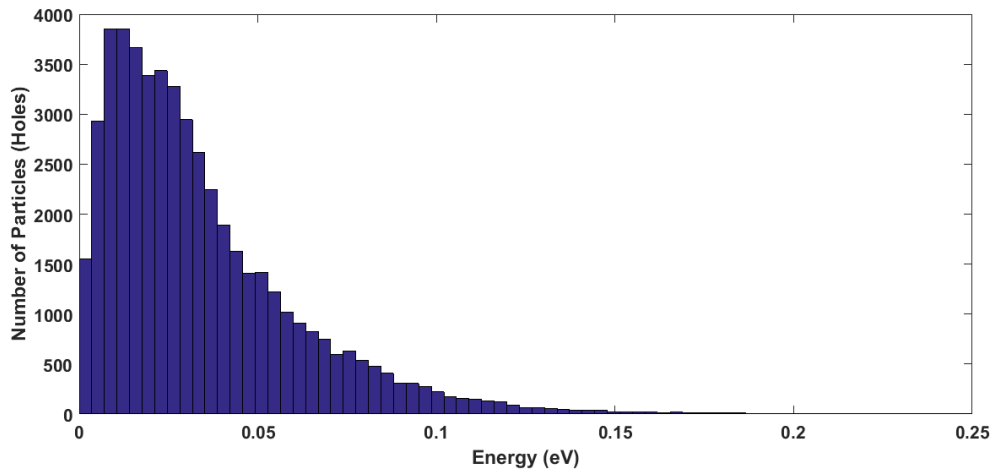


Figure 5.5: Histogram Showing the Final Carrier Energy Distribution at an Electric Field of $50 \frac{kV}{cm}$.

The shift in the distributions in the wave vector is evident from the results shown in Figures 5.6 , 5.7 and 5.8. This is again due to the applied electric field.

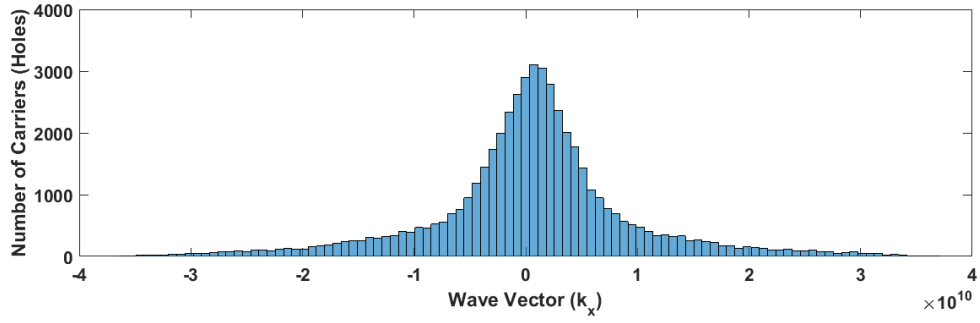


Figure 5.6: Histogram Showing the Final Carrier Wave Vector (k_x) Distribution at an Electric Field of $50 \frac{kV}{cm}$

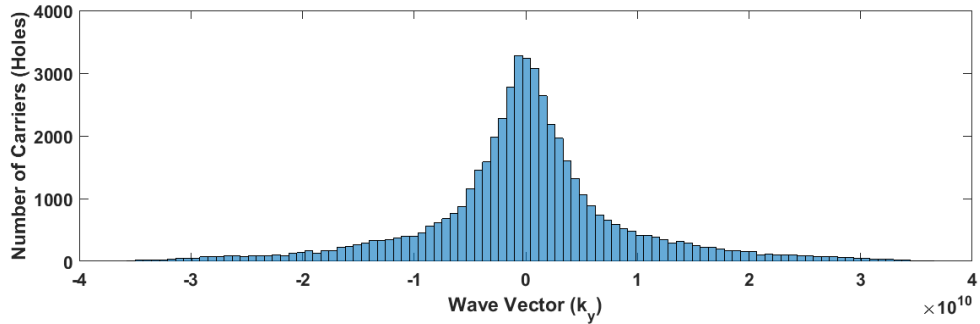


Figure 5.7: Histogram Showing the Final Carrier Wave Vector (k_y) Distribution at an Electric Field of $50 \frac{Kv}{cm}$

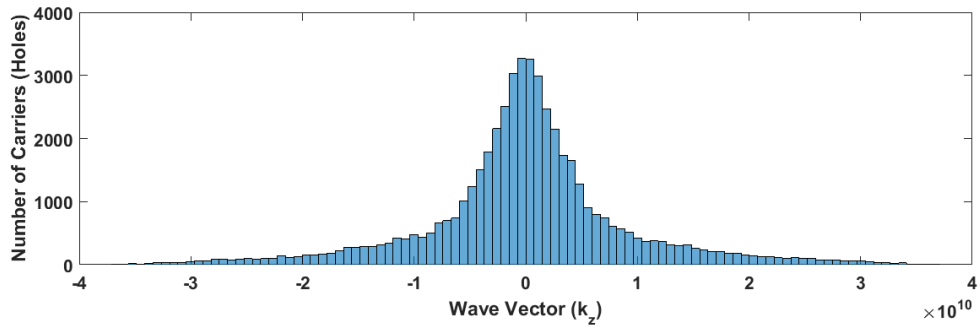


Figure 5.8: Histogram Showing the Final Carrier Wave Vector (k_z) Distribution at an Electric Field of $50 \frac{Kv}{cm}$

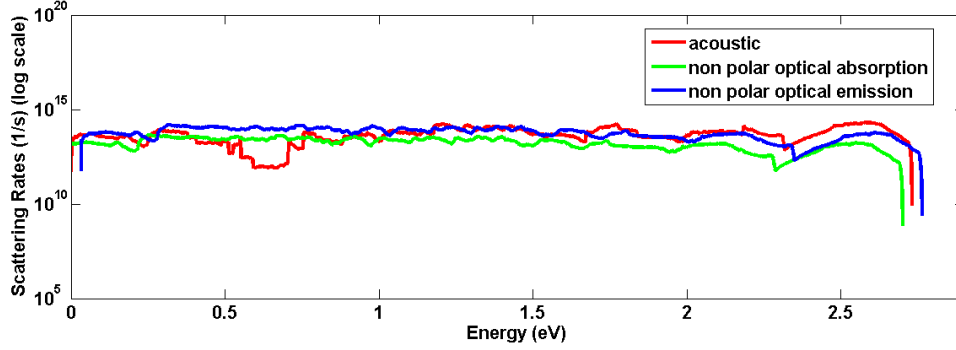


Figure 5.9: Scattering Rates (1/s) in Log Scale vs. Energy

5.3 Scattering Rates

Figure 5.9 shows all the scattering rates in one single plot. Non-polar optical phonon emission scattering dominates at lower energies.

5.4 Energy and Velocity vs. Time Characteristics

In Figures 5.10 and 5.11 the plots for drift velocity vs time and energy vs time are shown . In both cases saturation is reached in a few picoseconds (for 600 kV/cm the energy saturates at around 15 picoseconds) and the saturation value increases with increase in the electric field.

5.5 Energy and Velocity vs. Electric Field Characteristics

The energy vs. electric field characteristics have been plotted for a range of electric fields between $(1 - 1000 \frac{kV}{cm})$.

The low field mobility is obtained from the slope of the velocity vs. field plot. From Figure 5.12, the low field hole mobility was calculated to be $5.51 \frac{cm^2}{Vs}$ at room temperature. The experimental value for low field hole mobility is $7.29 \frac{cm^2}{Vs}$ [40].

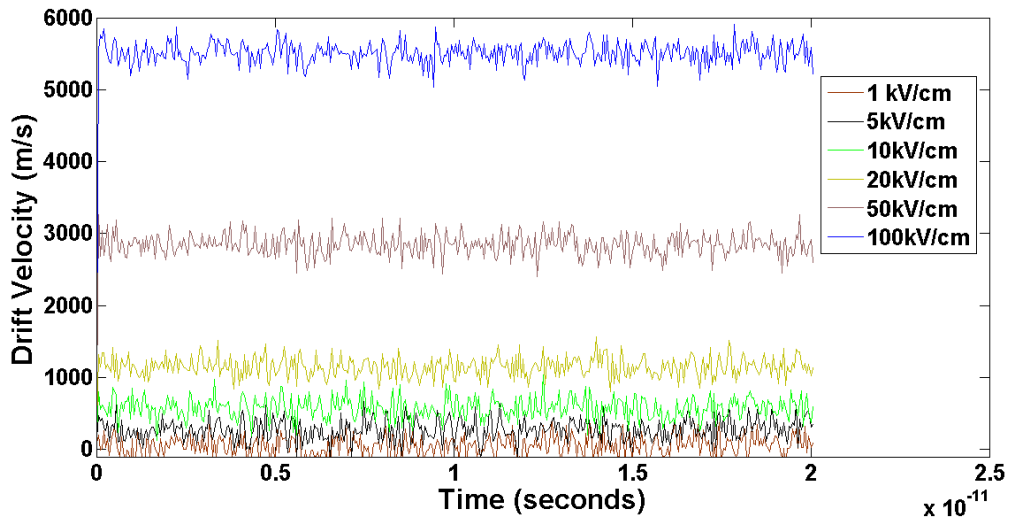


Figure 5.10: Drift Velocity vs. Time Characteristics.

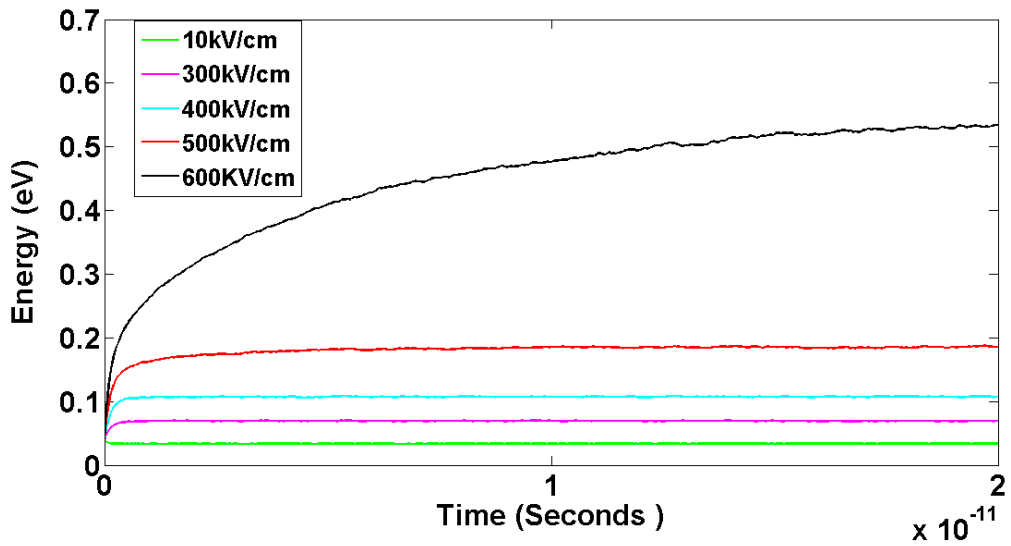


Figure 5.11: Energy vs. Time Characteristics.

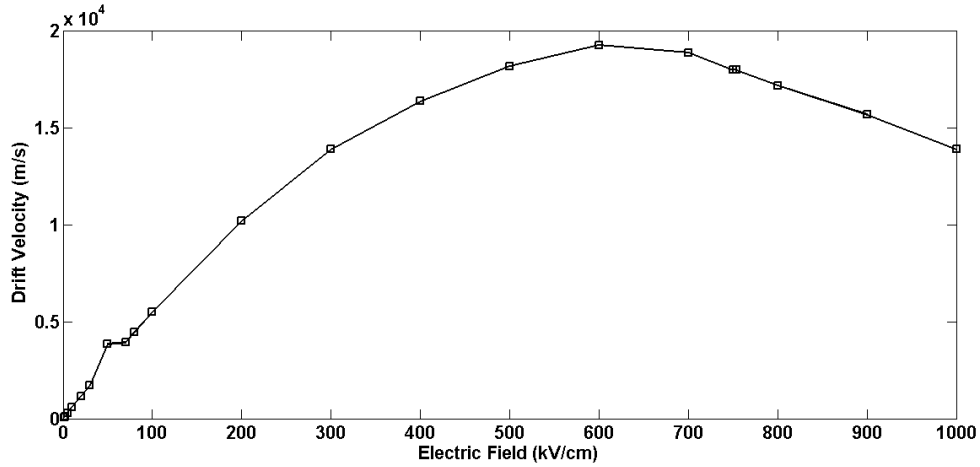


Figure 5.12: Drift Velocity vs. Electric Field

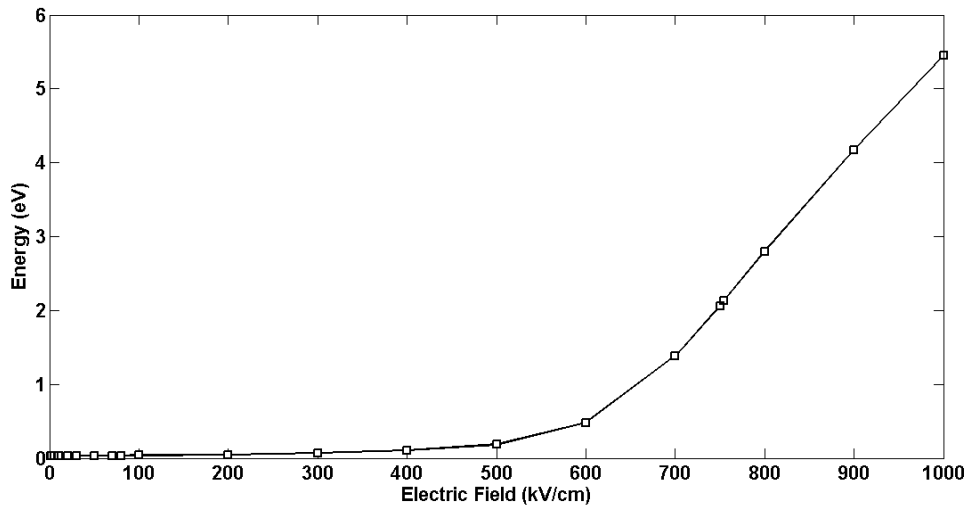


Figure 5.13: Energy vs. High Electric Field

In Figure 5.13 we show the change in average ensemble energy with change in electric field.. Tsuji et al. [41] have experimentally shown that the ionization threshold energy in a-selenium is 2.1eV. From Figure 5.13 we have calculated the electric field at which the average energy of carriers is 2.1eV. It is here that we have used the effective mass of holes as a fitting parameter to match the experimental onset of

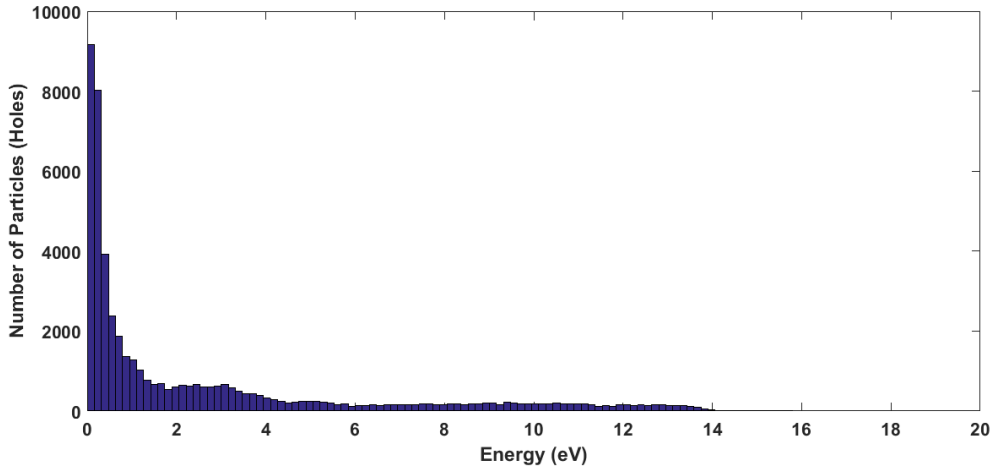


Figure 5.14: Histogram Showing the Final Carrier (Hole) Distribution at the Break-down Field of $754 \frac{kV}{cm}$. A Shift of Carriers into Higher Energies Can Be Seen Above.

breakdown to be $754 \frac{kV}{cm}$.

5.6 Mobility vs. Temperature

Finally, we present the Arrhenius Plot for Mobility vs. temperature and compare it with experimental data [40]. The lattice mobility of holes in a single-crystalline monoclinic selenium at room temperature is $8 \frac{cm^2}{V.s}$. Although this band mobility has not been measured in Se, due to the intrinsic meta-stability of the monoclinic phase and high trap density in prepared specimens, comparison to measured non-activated band mobilities in pure Sulphur (S) orthorhombic crystals validates this estimation. Figure 5.15 shows measured activated trap-limited mobility Arrhenius plot for holes in both monoclinic Se and orthorhombic S specimens where fitted lines were calculated using the multiple-trapping model and the interaction of drifting hole carriers with shallow traps via capture and thermal release events [42, 43, 44]. As the trap densities increase in Orthorhombic sulphur, the mobility decreases as the transport

shifts from band transport via extended states to activated trap limited mobility . The samples of monoclinic selenium namely A and B contained too high a density of shallow defect centres for the observation of drift mobility [45, 46].

Given the similarities between Se and S in terms of (1) hole band structure (i.e., valence band), (2) puckered 8-atom ring molecular symmetry (i.e., similar bond length, bond angle, and dihedral angle), and (3) activation energies of trap-limited hole mobilities, one can also estimate the same room-temperature band mobility of $8 \frac{cm^2}{V.s}$ for holes in Se as that of measured non-activated hole mobility in pure S crystals. Note that measured non-activated band mobilities of holes in S crystals with low trap densities are shown in Fig. 5.15 where mobility increases with decreasing temperature and the trend is further extrapolated with a dash line over a wider temperature range. We simulated the lattice band mobility for holes in Se using Monte-Carlo simulation of the BTE and our non-activated mobility values are in close agreement with measurement. In a-selenium, at high electric fields holes travel via the extended states and thus trapping effects are not activated. This explains, not taking shallow trap states into account and the deviation from experimental results . The deviation gets more severe as we move to lower temperatures where conduction is primarily via activated transport.

5.7 Conclusions

Thus we have modeled m-selenium to study the transport properties of a-selenium. To summarize, we started with calculating the band structure and DOS function for m-selenium. Next we created a scattering table based on the DOS function, which included acoustic and non polar optical phonon scattering as the dominant scattering

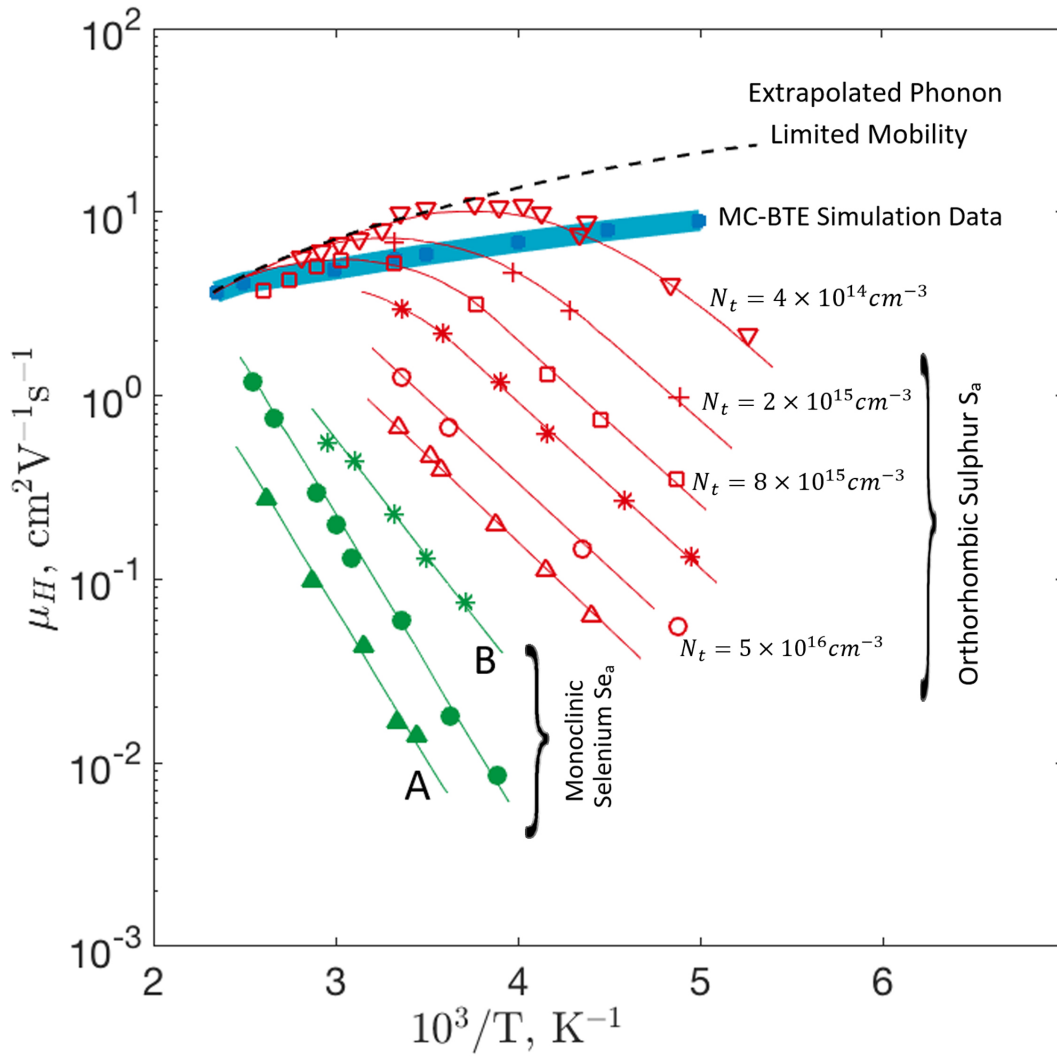


Figure 5.15: Arrhenius Plot for Mobility (Log Scale) vs. Temperature.

Table 5.2: A Comparison Between Experimental and Simulated Mobility for M-selenium Tabulated Against Temperature.

Arrhenius plot x-axis ($\frac{10^3}{T}$)	Temperature (K)	Simulation($\frac{cm^2}{Vs}$)	Experiment($\frac{cm^2}{Vs}$)
3.5	285	5.844	8.29
3.3	300	5.51	7.29
3	333	4.86	5.518
2.5	400	4.12	4.02
2.347	426	3.657	3.637

mechanisms in m-selenium. Finally we studied the transport properties in m-selenium using a bulk MC method and plotted the energy/velocity vs. time, energy/velocity vs. electric field and mobility vs. temperature results.

Our simulated mobility at room temperature ($5.51 \frac{cm^2}{Vs}$) is close to the experimental value ($7.29 \frac{cm^2}{Vs}$). Moreover, the Arrhenius plot for mobility vs. temperature is a close fit to experimental values.

In the present work, we have treated acoustic scattering under the elastic and equipartition approximation. In the future, we will calculate acoustic scattering outside the elastic and equipartition approximation which gets violated at low temperatures. Thus we will treat emission and absorption processes separately. Moreover, we will add Coulomb scattering to take into account scattering due to impurities in the material and model a full-band Monte Carlo algorithm so as to eliminate the need to use effective mass as a fitting parameter.

BIBLIOGRAPHY

- [1] A. D. Grigorovici, N. Croitoru and E. Teleman, “Band structure and electrical conductivity in amorphous germanium,” *Proe. International Conf. on Physics of Semiconductors*, pp. 423–428, Paris 1964.
- [2] R. A. Street, *Hydrogenated Amorphous Silicon*. Cambridge University Press., 2005.
- [3] L. Banyai, “Band structure and the theory of electric conduction in amorphous semiconductors,” *Proe. Inttmlltional Conf. on Physics of Semiconductors*, pp. 417–421, Paris,1964.
- [4] H. Dessauer and H. E. Clark, *Xerography and Related Processes*. Focal Press,New York, 1965.
- [5] S. R. Ovshinsky and H. Fritzsche *IEEE Trans. Electron Devices*, vol. 20, p. 91, 1973.
- [6] D. Adler and N. F. Mott *Rev. Mod. Phys*, vol. 50, p. 209, 1978.
- [7] J. N. Wolfe, *Xeroradiography of the Breast*. 2nd ed , C.C. Thomas, Springfield, IL, 1983.
- [8] K. Nomura, H. Ohta, A. Takagi, T. Kamiya, A. Hirano, and H. Hosono *Nature*, vol. 432, p. 488, 2004.
- [9] S. Iftiquar, J. Jung, H. Park, J. Cho, C. Shin, J. Park, J. Jung, S. Bong, S. Kim, and J. Yi, “Effect of light trapping in an amorphous silicon solar cell,” *Thin Solid Films*, vol. 587, pp. 117–125, July 2015.
- [10] G. C. Fletcher, *The electron band theory of solids*. Amsterdam: Noord-Hollandsche U.M., 1971.
- [11] K. Moorjani and C. Feldman, “Electrical properties of amorphous semiconductors,” *Reviews of Modern Physics*, vol. 36, no. 4, pp. 1042–1049, 1964.
- [12] A. I. Gubanov, *Quantum electron theory of amorphous conductors*. New York: Consultants Bureau, 1965.
- [13] S. Makinson and A. Roberts, “Zone theory of liquids,” *Australian J.Phys.*, vol. 13, pp. 437–445, 1960.
- [14] S. Makinson and A. Roberts, “Existence of energy gaps in one-dimensional liquids,” *Proc. Phys. Soc.*, vol. 78, pp. 926–931, 1961.
- [15] H. Budd *In Proceedings of the International Conference on the Physics of Semiconductors, Kyoto, J. Phys. Soc. Jpn. Suppl*, vol. 21, p. 420, 1966.
- [16] W. Fawcett, D. Boardman, and S. Swain *J. Phys. Chem. Solids.*, vol. 31, 1963.

- [17] P. J. Price *In Proceedings of the 9th International Conference on the Physics of Semiconductors*, edited by S. M. Ryvkin, p. 173, 1968.
- [18] T. Kurosawa *in Proceedings of the International Conference on the Physics of Semiconductors, Kyoto, J. Phys. Soc. Jpn. Suppl.*, vol. 21, p. 424, 1966.
- [19] Buslenko, Golenko, Schrieder, Sobol, and Sragovich, “The monte carlo method: the method of statistical trials,” 1966.
- [20] A. Goldan, “Unipolar charge-sensing for evaporated large-area solid-state photoconductors for digital radiography.,” *PhD Thesis, UWSpace*, 2012.
- [21] J. Rowlands and S. Kasap, “Amorphous Semiconductors Usher in Digital X-Ray Imaging,” *Physics Today*, vol. 50, no. 11, p. 24, 1997.
- [22] A. H. Goldan, C. Li, S. J. Pennycook, J. Schneider, and W. Zhao, “Molecular structure of vapor-deposited amorphous selenium,” *Journal of Applied Physics*, vol. 120, no. 13, 2016.
- [23] “Direct conversion x-ray detectors,” <https://www.analogic.com/products/digital-mammography/direct-conversion-x-ray-detectors/>.
- [24] A. Goldan, J. Rowlands, M. Lu, and W. Zhao, “Nanopattern multiwell avalanche selenium detector with picosecond time resolution,” *IEEE Nuclear Science Symposium and Medical Imaging Conference*, pp. N32–N34, Seattle, 2014.
- [25] A. F. Ioffe and R. Regel, “Non-crystalline, amorphous and liquid electronic semiconductors,” vol. 4, pp. 237–291, 1960.
- [26] N. F. Mott and W. D. Twose, “Theory of impurity conduction,” *Adv. Phys.* 10, 1961 , 107-163.
- [27] A. Goldan, J. Rowlands, Tousignant, and K. Karim, “Unipolar time-differential charge sensing in non-dispersive amorphous solids.,” *Journal of Applied Physics*, vol. 113, pp. 224–502, 2013.
- [28] K. Koughia, S. Shakoor, Z. Kasap, and J. Marshall *J. Appl. Phys.* 97, 033706 .2005, vol. 97, p. 706, 2005.
- [29] M. Kastner and P. H. Fritzsche *Philosophical Magazine BMag.*, vol. B37, p. 199, 1978.
- [30] F. Mott, E. Davis, and R. Street *Philosophical Magazine BMag.*, vol. B32, p. 961, 1975.
- [31] “Virtual nanolab version 2017.1, quantumwise a/s,” www.quantumwise.com.
- [32] “Quantumwise website, atk manual , atomic-scale simulators , technical notes,” <https://docs.quantumwise.com/manuals/technicalnotes/>.
- [33] M. V. Fischetti, “Monte carlo solution to the problem of high-field electron heating in SiO_2 ,” *Physical Review Papers, Volume 53 , Number 18 , 1984*.

- [34] M. Fischetti, D. DiMaria, S. Brorson, T. Theis, and J. Kirtley, “Theory of high-field electron transport in silicon dioxide,” *Physical Review B*, vol. 31, p. Number 12, 1985.
- [35] D. Vasileska, S. Goodnick, and G. Klimeck, *Computational electronics : semi-classical and quantum device modeling and simulation*. Boca Raton, FL: CRC Press, Taylor Francis Group, 2010.
- [36] O. Rubel and D. Laughton, “Lone-pair states as a key to understanding impact ionization in chalcogenide semiconductors,” *Journal of physics. Condensed matter : an Institute of Physics journal*, vol. 22, September 2010.
- [37] J. P. McKelvey *Solid State and Semiconductor Physics (Krieger, Malabar, Florida, 1982)*.
- [38] D. Vasileska and S. Goodnick, *Computational electronics*. Synthesis lectures on computational electromagnetics (Online), 6, San Rafael, Calif.: Morgan amp; Claypool Publishers, 1st ed. ed., 2006.
- [39] H. D. Rees *J. Phys. Chem. Solids*, vol. 30, p. 643, 1960.
- [40] F. Dalrymple and W. Spear, “A comparison between the electronic structure of orthorhombin sulphur and monoclinic selenium.,” *J. Phys. Chem. Solids*, vol. 33, pp. 1071–1078, 1972.
- [41] K. Tsuji, Y. Takasaki, T. Hirai, and K. Taketoshi, “Impact ionization process in amorphous selenium,” *Journal of Non-Crystalline Solids*, vol. 144, pp. 94–96, North-Holland, 1989.
- [42] T. Tiedje and A. Rose, “A physical interpretation of dispersive transport in disordered semiconductors,” *Solid State Communications*, vol. 37, no. 1, pp. 49–52, 1981.
- [43] W. Spear, “Drift mobility techniques for the study of electrical transport properties in insulating solids,” *Journal of Non-Crystalline Solids*, vol. 1, no. 3, pp. 197–214, 1969.
- [44] J. Noolandi, “Multiple-trapping model of anomalous transit-time dispersion in a-Se,” *Physical Review B*, vol. 16, no. 10, pp. 4466–4473, 1977.
- [45] W. Spear *J. Phys. Chem. Solids*, vol. 21, p. 110, 1961.
- [46] J. Caywood and C. Mead *J. Phys. Chem. Solids*, vol. 31, p. 983, 1970.